Oxidation s

tate of iron

in hydrous phono-tephritic melts

JAN A. SCHUESSLER[1*], ROMAN E. BOTCHARNIKOV[1], HARALD BEHRENS[1],

VALERIA MISITI[2] AND CARMELA FREDA[2]

[1] Institut für Mineralogie, Leibniz Universität Hannover, Callinstr. 3, D-30167 Hannover, Germany

[2] Istituto Nazionale di Geofisica e Vulcanologia, Sezione di Sismologia e Tettonofisica, Via di Vigna Murata 605, Rome, I-00143, Italy

revised manuscript 2795R

to be published in

American Mineralogist

"Virtual Special Issue": Frontiers in Mineral Sciences 2007

14 January 2007

* - corresponding author

e-mail: j.schuessler@mineralogie.uni-hannover.de

ABSTRACT

The oxidation state of iron in hydrous ultrapotassic (phono-tephritic) melts coexisting with mixed H_2O-CO_2 fluids was experimentally studied at 1200 and 1250°C and pressures from 50 to 500 MPa. The oxygen fugacity (f_{O_2}) varied from NNO–2.9 to NNO+2.6 in log f_{O_2}, relative to the Ni-NiO oxygen buffer (NNO), as imposed by external redox conditions in experimental vessels and internal variations in water activity from 0.05 to 1 inside the capsules. The iron redox state of the quenched melts was determined by colorimetric wet-chemical analysis. This analytical method was optimized to measure the $Fe^{2+}/\Sigma Fe$ ratio of mg-sized samples within ±0.03 (2σ). The accuracy and precision was tested with international reference materials and with standards analyzed by other methods. The $Fe^{2+}/\Sigma Fe$ ratio of the experimental glasses covered a range of 0.41 to 0.85. A small negative effect of dissolved water on $Fe^{2+}/\Sigma Fe$ at given f_{O_2} was found, consistent with the thermodynamic model of Moretti (2005). No effect of pressure and temperature on the redox state of iron was resolvable in the investigated P-T range. Compared to hydrous ferrobasaltic melts that were studied previously under similar conditions, systematically lower $Fe^{2+}/\Sigma Fe$ ratios were found for the phono-tephritic melts, in particular at low oxygen fugacities. This effect is attributed to the much higher K_2O contents of the phono-tephrite (7.5 compared to 0.3 wt%), but the difference in ΣFeO (7.8 wt% in the phono-tephrite and 12.9 wt% in the ferrobasalt) may have an influence as well. Comparison of the experimentally obtained relationship between log f_{O_2} and Fe^{3+}/Fe^{2+} for the studied hydrous ultrapotassic melts with commonly used empirical and thermodynamic models suggest that these models can be successfully applied to phono-tephritc melts, although such compositions were not implemented in the model calibrations. Furthermore, the new data can be used to improve the models with respect to the effects of compositional variables, such as H_2O or K_2O, on the redox state of iron in silicate melts.

Keywords: iron oxidation state, ferrous iron determination, oxygen fugacity, water activity, phono-tephrite, ultrapotassic hydrous silicate melt, Alban Hills

INTRODUCTION

The oxidation state of iron varies widely in natural magmas (e.g., Carmichael, 1991) and influences their physical and chemical properties as well as the phase equilibria for iron-bearing minerals. The redox state of iron in the melt is related to the oxygen fugacity via the reaction $Fe(II)O_{melt} + ¼\ O_{2\ gas} = Fe(III)O_{1.5\ melt}$ and the equilibrium constant of the reaction can be expressed as $K = a_{Fe(III)O_{1.5}} / (a_{Fe(II)O} \cdot (a_{O_2})^{¼})$ where *a* denotes the activity of the respective components in the melt. *K* depends on temperature, pressure and melt composition. Knowledge of the Fe redox state in magmas is a pre-requisite to understand the physical and chemical properties of magmas, to constrain source regions of magmas and their redox states, and the processes occurring during magma genesis and evolution. Specifically, the redox state of iron has influence on the stability of iron bearing minerals that may crystallize during magma evolution, and hence, control the iron content of the residual melt, and the stability and composition of major silicate phases (e.g., Pichavant et al., 2002). Furthermore, the structural incorporation of ferric and ferrous iron in silicate melts may affect the viscosity of a magma (e.g., Liebske et al.; 2003; Vetere et al., 2006), which has strong influence on the dynamics of volcanic eruptions. In particular, interaction between various species of different elements may influence the partitioning of volatile elements between silicate melts and coexisting gas phases, which strongly affects the degassing behavior of ascending magmas (e.g., Moretti and Ottonello, 2003; Moretti and Papale, 2004; Burgisser and Scaillet, 2007).

Several empirical relations have been proposed to quantify the effect of various parameters on the Fe redox state in silicate melts and to predict the prevailing oxygen

fugacity in a magmatic system from Fe redox ratios of quenched melts (e.g., Sack et al., 1980; Kilinc et al., 1983; Kress and Carmichael, 1988; Mysen, 1988; Borisov and Shapkin, 1989; Kress and Carmichael, 1991; Nikolaev et al., 1996; Jayasuriya et al., 2004). The early empirical models were calibrated over a relatively wide range of melt compositions, temperatures and oxygen fugacities, but the data basis comprised dry silicate melts only. Subsequent experimental investigations on silicate melts of different chemical compositions and also on hydrous silicate melts revealed in part considerable discrepancies between predicted Fe^{2+}/Fe^{3+} ratios of the melts and experimental findings (Sisson and Grove, 1993; Moore et al., 1995; Baker and Rutherford, 1996; Gaillard et al., 2001; Wilke et al., 2002; Gaillard et al., 2003; Partzsch et al., 2004; Botcharnikov et al., 2005). The deviations might be either due to ignoring the component H_2O in the empirical models or due to differences in anhydrous melt compositions studied in the experiments compared to the compositions used to calibrate the models. As an alternative, a thermodynamic model based on a polymeric approach was developed for the prediction of the Fe redox state in dry silicate melts at atmospheric pressures by Ottonello et al. (2001). Recently, this model was extended by Moretti (2005) to account for the effects of dissolved water and pressure.

Here we use samples from a previous study on volatile solubility in phono-tephritic melts (Misiti et al., this issue) to test the predictive power of commonly used models for Fe^{2+}/Fe^{3+} ratios in ultrapotassic silicate melts because hydrous phono-tephritic melts have not been used in the calibration of those models. A positive effect of increasing K_2O on the $Fe^{2+}/\Sigma Fe$ has been proposed by Tangeman et al. (2001) for dry iron-rich K_2O-FeO-Fe_2O_3-SiO_2 liquids at atmospheric pressure, whereas other studies

98 suggest a stabilization of tetrahedrally coordinated ferric iron by charge-balancing K_2O (
99 Sack et al., 1980; Kilinc et al., 1983; Dickenson and Hess, 1986; Kress and Carmichael,
100 1988). To date, no experimental data exists on hydrous K_2O-rich melts at elevated
101 pressures. The new data allow us to investigate the influence of water activity and oxygen
102 fugacity on the redox state of iron in the melts as well as to evaluate the compositional
103 effects of water, potassium and total iron content on the $Fe^{2+}/\Sigma Fe$ ratio. The results are
104 compared to the widely used empirical model of Kress and Carmichael (1991) and the
105 thermodynamic model of Moretti (2005).
106
107 **EXPERIMENTAL METHODS**
108 The experimental strategies and procedures are described in detail in Misiti et al.
109 (this issue) and are summarized briefly here. The starting material for the experiments
110 was a synthetic analogue of the phono-tephritic Mt. Mellone lava flow composition from
111 the Alban Hills Volcanic District in Central Italy (Marra et al., 2003; Gaeta et al., 2006).
112 For each experiment ~50 mg glass powder, 0 to 20 μL deionised water and 0 to 15 mg
113 silver oxalate ($Ag_2C_2O_4$) were sealed in $Au_{80}Pd_{20}$ capsules (~15 mm length, 2.6 mm inner
114 diameter, 0.2 mm wall thickness). To reduce Fe loss to the capsule walls in the
115 experiments under reducing conditions the capsules were pre-saturated with Fe as
116 described in Botcharnikov et al. (2005). The experiments were performed in internally
117 heated gas pressure vessels (IHPV) at temperatures of 1200 and 1250°C and pressures
118 between 50 to 500 MPa for 1.5 to 72 hours (Table 1). Uncertainties in temperature and
119 pressure were ±10°C and ±5 MPa, respectively. Samples were rapidly quenched at the
120 end of the experiments with an initial cooling rate of about 150°C/s (Berndt et al., 2002).

121 Most of the experiments were performed at intrinsic redox conditions of the IHPV
122 pressurized with Ar. The intrinsic oxygen fugacity in capsules with pure H_2O fluid (mole
123 fraction of water in the fluid $X^f_{H_2O} = 1$) in the IHPV used in this study was determined by
124 NiPd-solid sensors (Taylor et al., 1992) at 1200°C and 200 MPa. The obtained value of
125 log f_{O_2} = -7.5 corresponds to NNO+2.6 (±0.5; 1σ from microprobe analyses of the NiPd
126 alloy) where NNO refers to the Ni-NiO buffer (Huebner and Sato, 1970). This f_{O_2} value is
127 about 0.9 log units lower than reported by Berndt et al. (2002) for a similar IHPV. The
128 difference reflects the uncertainty in f_{O_2} due to unbuffered hydrogen fugacity at intrinsic
129 conditions in the IHPV, i.e., the prevailing f_{H_2} depends on the specific components used
130 in the individual IHPV (furnace, sample holder, etc.).
131 Experiments at low f_{O_2} were performed in another IHPV pressurized with an Ar-
132 H_2 mixture. The IHPV is equipped with a Shaw-membrane to monitor the f_{H_2} at high
133 pressure and temperature (Berndt et al., 2002). The f_{H_2} controls the f_{O_2} in the capsule
134 through the equilibrium reaction $H_2 + ½ O_2 \leftrightarrow H_2O$. The accuracy of log f_{O_2} is estimated
135 to be ±0.2 log units for experiments with pure H_2O fluids. In experiments with mixed
136 H_2O-CO_2 fluids the fugacity of H_2O and hence the f_{O_2} is decreasing with increasing f_{CO_2}.
137 The prevailing f_{O_2} in the capsule was calculated from the fluid composition determined
138 after the experiment. Hence, differences in oxygen fugacity in capsules processed in the
139 same run are determined only by the differences in $X^f_{H_2O}$. The precision of the latter is
140 limited by the uncertainties associated with the weight-loss determination of H_2O and
141 CO_2 released from the capsules after the experiments. In this case the relative precision of

log f_{O_2} for experiments processed in the same run was estimated from error propagation of weighing uncertainties to be approximately ±0.1 log units. However, taking the uncertainty of the intrinsic redox condition in the IHPV into account, the error in absolute log f_{O_2} values of experiments processed in different runs is higher (approximately ±0.5 log units).

ANALYTICAL METHODS

The composition of the fluid phase in equilibrium with the silicate melt (expressed in mole fractions of H_2O and CO_2, $X^f_{H_2O}$ and $X^f_{CO_2}$, respectively) was determined by a conventional weight-loss technique. H_2O and CO_2 concentrations in the glasses were measured by FT-IR spectroscopy. Bulk H_2O contents of quenched melts were also measured by Karl-Fischer titration (KFT). Analytical details and results of these investigations are reported in Misiti et al. (this issue). Here, we focus on measurements relevant for the oxidation state of iron in the melt. The chemical compositions of the post-experimental glasses were determined by electron microprobe analysis (EMPA). The redox state of iron ($Fe^{2+}/\Sigma Fe$) was analyzed using a wet-chemical technique, which is based on the colorimetric method of Wilson (1960). Both techniques are described below.

Electron microprobe analysis

Glass fragments from representative samples were mounted in epoxy and polished for electron microprobe analysis. Analytical conditions were 5 nA, 15 kV and a beam diameter of 20 μm, with counting times of 8 s for Si, Al, Fe, Mg, Ca, Mn and Ti on the peak and 4 s on the background and 4 s for K and Na on the peak and 2 s on the

background to minimize the loss of alkalis. Cameca supplied standards were used for calibration and PAP matrix correction according to Pouchou and Pichoir (1991) was applied. Between 8 and 20 spot analyses were made on each sample to check for homogeneity of the glass compositions and analytical reproducibility. The results are listed in Table 2.

Ferrous iron analyses

Different wet-chemical techniques have been developed to determine the redox state of iron in geological materials, where most of them employ titration methods for quantification. Conventional techniques usually involve the acid dissolution of 100 to 500 mg of powdered sample material and subsequent precise determination of the absolute ferrous iron concentration. To obtain the $Fe^{2+}/\Sigma Fe$ ratio, the total iron concentration is commonly determined by an additional method, i.e., electron microprobe analysis or optical emission spectroscopy (ICP-OES). In experimental studies the amounts of samples are often limited to <50 mg and this material is subjected to several different analytical methods. This limits the amount of sample available for the wet-chemical ferrous iron determination. Here, we follow the colorimetric method of Wilson (1960) to measure the $Fe^{2+}/\Sigma Fe$ ratio in mg-sized samples after acid dissolution. The original method was modified to minimize handling of toxic materials (i.e., beryllium sulfate was replaced by boric acid, see below) and to improve the reproducibility. To asses the accuracy and precision of this method, we have analyzed international reference materials and in-house standards.

187 The critical point in ferrous iron analysis is to avoid an oxidation of Fe^{2+} during
188 the analytical procedure. Here, samples are decomposed in a HF-H_2SO_4 mixture in
189 presence of excess pentavalent vanadium, which oxidizes ferrous iron as soon as it is
190 released from the sample. According to the reaction

191 $$\overset{+5}{V}O_2^+ + 2H^+ + Fe^{2+} \rightleftharpoons \overset{+4}{V}O^{2+} + H_2O + Fe^{3+} \quad (1)$$

192 the amount of generated tetravalent vanadium, which is highly resistant to oxidation
193 compared to Fe^{2+}, is equivalent to the amount of Fe^{2+} in the sample. The equilibrium of
194 the reaction is shifted to the right hand side under the strongly acidic conditions during
195 sample dissolution (pH < 1). After complete sample dissolution ferrous iron is
196 regenerated from tetravalent vanadium by increasing the pH value to ~5, which shifts the
197 equilibrium of reaction (1) to the left hand side.

198 The analytical procedure is as follows (employed reagents are listed in
199 Appendix 1): The powdered sample (in case of references materials) or sub-millimeter-
200 sized glass fragments (from experimental products) were weighed into a 15-mL Savillex®
201 Teflon beaker containing 1 mL of an ammonium vanadate solution dissolved in sulfuric
202 acid (1*M* to 5*M* H_2SO_4). After addition of 1 mL HF (24 or 48%), the beakers were tightly
203 sealed and placed in an ultrasonic bath for about 15 minutes. Thereafter, the beakers were
204 left for 3 to 24 hours at temperatures between 20 to 100°C until complete sample
205 dissolution was attained. Acid concentrations, dissolution time and temperature were
206 systematically varied to test for potential effects of these parameters on the analytical
207 results (see discussion below). After sample dissolution, 5 mL saturated hot boric acid
208 solution (at ~80°C) was added, instead of beryllium sulfate as proposed by Wilson
209 (1960), to neutralize excess HF and to bring possibly formed fluorides back into solution.

Upon cooling to room temperature the content of the beaker was quantitatively transferred into a 100-mL volumetric flask, containing 10 mL ammonium acetate solution, 5 mL 2:2'bipyridyl solution, and the remaining volume was filled with distilled water. The ammonium acetate buffer adjusted the pH value to ~5. The regenerated Fe^{2+} forms a very stable complex with 2:2'bipyridyl in the solution which shows an intensive absorption band in the visible spectrum (Fig. 1).

Measurements of ferrous Fe and total Fe were made on the same solution before and after adding 5 to 10 mg solid hydroxylamine hydrochloride to an aliquot of about 10 mL. This reducing agent converts all ferric Fe into the ferrous state. Since both Fe^{2+} and total Fe are measured in the same solution, the $Fe^{2+}/\Sigma Fe$ ratio can be directly calculated by dividing the absorbances of the Fe^{2+} and total Fe aliquots. The advantage compared to an absolute concentration measurement of ferrous iron and an additional total Fe determination by another method (e.g., EMPA or ICP-OES) is that uncertainties in the $Fe^{2+}/\Sigma Fe$ ratios arise mainly from the spectrometric measurements, whereas weighing and dilution errors cancel out. Absolute concentrations were obtained as well after calibration of the spectrometric technique using ferrous ammonium sulfate solutions of different known Fe^{2+} concentrations. For all measurements 1 cm transmission cells and an UV/VIS spectrometer (Zeiss Specord S10*)* was used. The sample solutions show a characteristic absorption band of the Fe(II)-2:2'bipyridyl complex at about 523 nm (Fig. 1). The maximum peak height was determined relative to a baseline measured at 700 nm. No differences in the general appearance of the spectra and in the maximum peak position were observed between samples of different matrices, i.e. basaltic to rhyolitic rocks or pure Fe(II) solutions.

233 The results of the wet-chemical colorimetric iron analyses on international
234 reference materials and in-house standards are given in Table 3. To asses the accuracy of
235 the method, our results are compared to the recommended values obtained by other
236 studies (Govindaraju, 1994; Govindaraju, 1995; Liebske et al., 2003; Bertoldi et al.,
237 2007). There is good agreement between the recommended $Fe^{2+}/\Sigma Fe$ ratios and the values
238 obtained by this study (Fig. 2). Furthermore, the results for our in-house standard PU-3
239 are in good agreement with measurements reported by Liebske et al. (2003). They
240 analyzed a synthetic andesitic glass similar in composition and synthesis conditions to
241 our PU-3 sample (1600°C, air atmosphere). Noteworthy, the $Fe^{2+}/\Sigma Fe$ ratios obtained for
242 the granites GS-N and GA are significantly higher than the recommended values.
243 Furthermore, the ΣFeO values (ΣFeO refers to total iron expressed as wt% FeO) of those
244 samples are also systematically lower than the recommended values. The presence of
245 undissolved refractory minerals containing significant amounts of ferric iron may explain
246 the discrepancy for these particular samples. The experimental products analyzed in this
247 study consist primarily of glass, which is readily dissolved within a few hours at room
248 temperature. Thus, no attempts were made to optimize the method for analyses of highly
249 resistant minerals, although this would be principally possible given some minor
250 modifications and tests.

251 For the two reference materials, natural olivine and commercial ammonium
252 iron(II) sulfate hexahydrate, the expected $Fe^{2+}/\Sigma Fe$ ratios are close to unity (Table 3). The
253 measured values of 0.93±0.08 and 0.95±0.05 (2σ), respectively, are systematically lower,
254 while for the chlorite sample CA the reported value of 0.90±0.02 from Bertoldi et al.
255 (2007) is still well reproduced by our measurements (0.89±0.04). To test whether

256 exclusion of atmospheric oxygen improves the recovery yield, some samples were
257 dissolved under Ar atmosphere, but no difference in the $Fe^{2+}/\Sigma Fe$ ratios was found.
258 Whipple (1974) and later Yokoyama and Nakamura (2002) noted that variable
259 concentrations of sulphuric acid and hydrofluoric acid may affect the accuracy of the
260 measured $Fe^{2+}/\Sigma Fe$ ratio as well. We have varied acid concentrations in the range from
261 1*M* to 5*M* H_2SO_4 and 24% to 48% HF, respectively, but did not observe any systematic
262 bias of the results. The potential effect of sample decomposition temperature on the
263 $Fe^{2+}/\Sigma Fe$ ratio was also studied (Table 3), since the dissolution kinetics at room
264 temperature could be more sluggish for some rock samples. Results obtained from
265 samples dissolved at 25°C are indistinguishable from those at 100°C, except for the
266 granitic sample GS-N, as discussed above.
267 The precision of the method can be evaluated from replicate measurements (Table
268 3). Reproducibility was between ±0.01 and ±0.05 (2σ) in the $Fe^{2+}/\Sigma Fe$ ratio for different
269 rocks and minerals containing between 1 and 8 wt% ferrous FeO. The long term
270 reproducibility (over a time period of about one year) was assessed from n = 33 replicate
271 analyses of the synthetic andesitic glass PU-3. Based on these measurements the
272 uncertainty of the $Fe^{2+}/\Sigma Fe$ ratios is ±0.03 (2σ, external precision). Despite the low
273 sample mass used for wet-chemical analyses, the obtained ΣFeO agree well with electron
274 microprobe analyses for experimental products and recommended values for the
275 reference materials, most of them within <5% relative (Tables 1, 2 and 3). Thus, we
276 conclude that the $Fe^{2+}/\Sigma Fe$ ratio can be reliably determined in the range from 0.4 to 0.9
277 by our method. All $Fe^{2+}/\Sigma Fe$ ratios of our experimental run products fall within this
278 range. Procedural blanks were always below the detection limit of the method, i.e. <0.012

absorbance units (3σ of the background), which corresponds to less than 1 µg Fe. This can be considered negligible relative to the processed amount of iron (100 to 500 µg Fe), since the maximum bias in the measured $Fe^{2+}/\Sigma Fe$ would be <0.01.

RESULTS

Except for one sample (Alb1-1) with very low water content, which was probably at the liquidus and thus partially crystallized, all experiments with less than 6 wt% of dissolved water in the melt yielded only glass and a fluid phase as experimental products. All melts with higher water contents contained crystals after quench. These crystals show typical features of non-equilibrium growth and were probably formed during quenching. The crystals were too small for a reliable quantitative microprobe analysis but semi-quantitative results, obtained by energy dispersive x-ray analyses (EDX), indicate a K-rich, Fe-bearing composition. X-ray powder diffraction on sample Alb1-5 gives evidence that the quench phases are mica. In experimental studies investigating basaltic melts under similar conditions and with similar experimental equipment no quench crystals were observed (e.g., Berndt et al., 2002; Botcharnikov et al., 2005). This discrepancy may be explained by the high potassium content of the phono-tephrite facilitating K-rich mica crystallization from a H_2O-rich melt of relatively low viscosity during cooling.

The results of electron microprobe analyses of representative post experimental glasses are given in Table 2. Sample Alb1-5 consists of glass and numerous quench crystals. Thus, the analyses were performed using a defocused electron beam (20 µm) and represent the bulk composition. After normalizing to a sum of 100 wt% (i.e.,

anhydrous composition) most of the glass compositions are identical to the starting glass (Alb1) and electron microprobe analyses show homogeneous ΣFeO concentrations in the glasses. Furthermore, from these data no indication for extensive dissolution of cations from the melt into the fluid phase is given. However, some samples (Alb1-1, Alb1-6a, Alb1-6bis, Alb1-H45, Alb1-H47 to Alb1-H51, Alb1-H56) have significantly lower ΣFeO (compare ΣFeO norm in Table 2 for samples with different water contents). These experiments were carried out under the most reducing conditions and at the lowest a_{H_2O}. At these conditions iron from the samples was partly dissolved as metallic Fe alloy in the capsule walls. As a consequence of the reduction of ferric and ferrous iron from the melt a small amount of oxygen was produced which reacted with hydrogen permeating from the pressure medium into the capsule forming some additional H_2O. The generated H_2O might have continuously increased the water activity and hence the oxygen fugacity within the capsule. The largest iron loss was observed for sample Alb1-H51 with a final ΣFeO of ~4.2 wt%. The corresponding increase in water content of the system is expected to be ~0.5 mg. Considering the masses of glass, fluid and the partitioning of H_2O between fluid and melt, f_{O_2} might have been increased by about half a log unit during the experiment. The rate of iron reduction is controlled most likely by the sluggish diffusion of Fe in the silicate melt. Fe diffusion is much slower than water and hydrogen diffusion in the melt (Gaillard et al., 2002; Behrens et al., 2004; Watson and Baxter, 2007) and, therefore, we suggest that $Fe^{2+}/\Sigma Fe$ is in near-equilibrium with the oxygen fugacity imposed by the fluid via the reaction $2\ Fe(II)O + H_2O = Fe(III)_2O_3 + H_2$.

Redox state of iron

The results of Fe redox analyses of the experimental run products are given in Table l. The measured $Fe^{2+}/\Sigma Fe$ ratios range from 0.41 at 1250°C, 200 MPa, NNO+2.6 (Alb1-15) to 0.85 at 1200°C, 200 MPa, NNO-2.9. A comparison of run P and run Q at 1200°C, 200 MPa with durations of 5 and 1.5 hours, respectively, reveals consistent results in terms of the redox state of iron. This finding and the homogeneous Fe concentration in the run products (Table 3) suggest that the system is close to equilibrium, in terms of both chemical and redox equilibrium, after 1.5 hours at 1200°C. This is also consistent with a study on Fe redox kinetics in peralkaline hydrous rhyolitic melts (Gaillard et al., 2002), revealing that redox kinetics are fast enough to equilibrate the melt within 3 hours at 800°C, but slow enough to readily quench the $Fe^{2+}/\Sigma Fe$ ratio of the melt in the experiments.

As mentioned above some samples are partially crystallized. Since the $Fe^{2+}/\Sigma Fe$ analyses were done upon complete dissolution of fragments of the experimental products (including quench crystals) they represent bulk values for the quenched melts, assuming that the bulk $Fe^{2+}/\Sigma Fe$ of the system is not significantly altered due to crystallization of Fe bearing mica during cooling. Despite an almost instantaneous permeation of H_2 from the pressure medium through the capsule walls and a transfer of Fe from the melt to the crystals during cooling, at an initial quench rate of about 150°C/s only a few seconds remain for a potential re-equilibration of the melt until the kinetics of the systems can be considered as virtually frozen, i.e., at T <500°C. During this time interval no significant change in the bulk $Fe^{2+}/\Sigma Fe$ ratio is expected from redox kinetics (Gaillard et al., 2002)

and thus the measured Fe redox ratios are considered to represent close-to-equilibrium values.

As shown in Figure 3, the $Fe^{2+}/\Sigma Fe$ ratio decreases nonlinearly with increasing mole fraction of water in the coexisting fluid phase ($X^{f}_{H_2O}$). The change in $Fe^{2+}/\Sigma Fe$ with $X^{f}_{H_2O}$ is more marked at oxygen fugacities >NNO-0.2 compared to the series at <NNO-0.2. At constant temperature, pressure, $X^{f}_{H_2O}$ and water content, the $Fe^{2+}/\Sigma Fe$ ratio increases with decreasing f_{O_2} (e.g., compare experiments at 200 MPa, 1200°C and $a_{H_2O} = 1$, Table 1).

DISCUSSION

Influence of oxygen fugacity and dissolved water on the speciation of iron

The main factors controlling the oxygen fugacity in the system are the water activity in the capsule and the hydrogen fugacity (f_{H_2}) in the IHPV at given P, T and melt composition. Permeability of hydrogen through the capsule walls is high at our experimental conditions, facilitating f_{H_2} equilibration between the capsule interior and the vessel atmosphere. The time needed to permeate the amount of H_2 required for reduction of all ferric iron in the starting glass (Alb1 $Fe^{2+}/\Sigma Fe = 0.29$) is less than two minutes based on permeation data for Au tubes (Chou, 1986). The prevailing oxygen fugacity within the capsule is mainly determined by the dissociation reaction of water ($H_2O = H_2 + ½\ O_2$) for which the equilibrium constant can be expressed as

$$K_w = f_{H_2O} \Big/ f_{H_2} \cdot \left(f_{O_2} \right)^{0.5} \qquad (2)$$

368 and the logarithm of oxygen fugacity is given as
369
370 $$\log f_{O_2} = 2\log f_{H_2O} - 2\log f_{H_2} - 2\log Kw \quad (3)$$
371

372 K_w was derived from thermodynamic data of Robie et al. (1978). The water fugacity in
373 the capsule is the product of water activity (a_{H_2O}) and standard state water fugacity
374 ($f^0_{H_2O}$). If the experimental pressure is chosen as standard state, $f^0_{H_2O}$ equals the
375 fugacity of the pure H_2O fluid and the water activity is calculated as $a_{H_2O} = \gamma^f_{H_2O} \cdot X^f_{H_2O}$
376 where $\gamma^f_{H_2O}$ is the activity coefficient of H_2O in the fluid. Activity coefficients of H_2O for
377 mixed H_2O-CO_2 fluids were computed for given P, T, $X^f_{H_2O}$ after Aranovich and
378 Newton (1999) using molar volumes of pure H_2O and CO_2 from Pitzer and Sterner
379 (1994). These calculations are only valid assuming that H_2O and CO_2 are the dominant
380 species in the fluid, which is a reasonable assumption for most of our experimental
381 conditions (see Botcharnikov et al., 2006 and references therein). However, especially at
382 very reducing conditions other species (e.g., CO, H_2, CH_4) can become more abundant.
383 Except for sample Alb1-H56, no indication of an abrupt drop in CO_2 solubility in the
384 melts with decreasing f_{O_2} was observed (see Fig. 7 in Misiti et al., this issue), that would
385 indicate a change of the dominant carbon species in the fluid. The anomalously low CO_2
386 of sample Alb1-H56 concentration in the melt indicates a lower prevailing f_{CO_2} in the
387 capsule than calculated by mass balance. A value of ~0.38 is estimated for $X^f_{CO_2}$ from
388 the relation between CO_2 concentration in the melt and $X^f_{CO_2}$ in Fig. 7 of Misiti et al.
389 (this issue). Assuming that the additional fluid component is mainly CO (Holloway and
390 Blank, 1994), the fluid composition was recalculated to $X^f_{H_2O}$ ~0.04 and $X^f_{CO_2}$ ~0.58.

Based on the recalculated $X^{f}_{H_2O}$ the oxygen fugacity is NNO-2.9. For sample Alb1-1 the fluid composition could not be determined and $X^{f}_{H_2O}$ was estimated from the H_2O-CO_2 saturation curve at 500 MPa and 1200°C (Misiti et al., this issue). It has to be noted that the uncertainties in the so-derived molar fractions of the fluid components, and consequently in the calculated oxygen fugacities, are probably higher compared to samples where fluid compositions were directly measured by the weight-loss technique (see Experimental Methods section).

The calculated oxygen fugacities are listed in Table 1. Additionally, the difference relative to the Ni-NiO (ΔNNO) buffer is given (Huebner and Sato, 1970). This allows a direct comparison of the experiments equilibrated at different temperatures and pressures to evaluate the effect of f_{O_2} on the redox state of iron in the silicate melts. In Figure 4 the iron redox state (expressed as Fe^{3+}/Fe^{2+} ratio) is plotted as a function of oxygen fugacity (ΔNNO). The data show an almost linear trend. The scatter of the data is due to superimposed variations in water content and experimental pressure as discussed below. The experiment Alb1-1 deviates noticeably from the trend (Fig. 4). This sample with very low water content (0.94 wt% H_2O) contains clinopyroxene crystals that may bias the measured iron redox ratio. Therefore, this sample is not considered further on in the systematics of the Fe redox state of the melt.

As shown in Figure 5, the $Fe^{2+}/\Sigma Fe$ ratios determined for the phono-tephritic melts are in general agreement with the predictions of the models of Kress and Carmichael (1991) and Moretti (2005). The dependence of the Fe^{3+}/Fe^{2+} ratio on log f_{O_2} at pressures of 200 MPa and 500 MPa and temperatures of 1200°C and 1250°C is shown

413 in Figure 6. In such a plot, a slope of 0.25 is expected according to the reaction
414 $Fe(II)O_{melt} + ¼\ O_{2\ gas} = Fe(III)O_{1.5\ melt}$. This slope is also implemented in the
415 thermodynamic model of Moretti (2005), whereas Kress and Carmichael obtained a slope
416 close to 0.2 for their emprical modelling. Considering the experiments done at relatively
417 oxidizing conditions (IHPV intrinsic; f_{H_2} ~0.6; Fig. 6a, b, d), the slope defined by the data
418 points at given P, T and f_{H_2} is 0.31 (1200°C, 500 MPa), 0.28 (1250°C, 500 MPa) and
419 0.37 (1200°C, 500 MPa), respectively, which is much larger than expected. This finding
420 is consistent with a positive dependence of the Fe^{3+}/Fe^{2+} ratio on the H_2O concentration
421 (Fig. 6d) in the melt as suggested by Moretti (2005). The data obtained at 1200°C, 200
422 MPa (Fig. 6c) define a much smaller slope of 0.16. Here, it has to be noted that due to
423 different f_{H_2} the oxygen fugacity is not directly correlated with the water fugacity over the
424 entire experimental f_{O_2} range.

425 A comparison of our data for phono-tephrite with the results of Botcharnikov et
426 al. (2005) for ferrobasalt studied at similar conditions can be used to evaluate the effect of
427 chemical composition on the redox state of iron in mafic melts. The phono-tephrite has a
428 much higher K_2O content (0.3 *vs.* 7.5 wt%) and a lower ΣFeO content (12.9 *vs.* 7.8 wt%)
429 than the ferrobasalt (Table 2). The comparison between our experimental dataset at
430 1200°C and 200 MPa and the data from Botcharnikov et al. (2005) for hydrous
431 ferrobasaltic melts obtained at the same P-T conditions (Fig. 6c) reveal slightly higher
432 Fe^{3+}/Fe^{2+} ratios for the ultrapotassic hydrous melts relative to the ferrobasaltic melts. This
433 effect is more pronounced at lower f_{O_2} . From linear regressions through each of the two
434 datasets the differences in $Fe^{2+}/\Sigma Fe$ ratios can be quantified. At a log f_{O_2} of -9 the

435 $Fe^{2+}/\Sigma Fe$ ratio of the phono-tephrite is 0.08 lower than that of the ferrobasalt. At more
436 oxidizing conditions of log f_{O_2} = -5 this difference decreases to a value of 0.01. This trend
437 is consistent with the model of Kress and Carmichael (1991) which predicts a decrease in
438 the $Fe^{2+}/\Sigma Fe$ ratio with increasing K_2O. For an increase from 0.3 to 8 wt% K_2O
439 (ferrobasalt *vs*. phono-tephrite) at 1200°C, 200 MPa and log f_{O_2} = -5 a decrease in
440 $Fe^{2+}/\Sigma Fe$ by 0.05 is calculated. The corresponding increase at log f_{O_2} = -9 is only 0.03.
441 Within this log f_{O_2} range and at water contents between 0 to 5 wt% in the melts, the
442 model of Moretti (2005) predicts no significant variation in $Fe^{2+}/\Sigma Fe$ with changing K_2O
443 (i.e., <0.003). If the ΣFeO content is reduced from 13 wt% to 8 wt% (ferrobasalt *vs*.
444 phono-tephrite), the decrease in the $Fe^{2+}/\Sigma Fe$ ratio calculated by the model of Kress and
445 Carmichael (1991) is 0.02 and 0.01 at log f_{O_2} of -9 and -5, respectively. Again, no
446 significant variation (<0.005) is predicted by the model of Moretti (2005). In conclusion,
447 both an increase of K_2O and a decrease of ΣFeO are predicted by Kress and Carmichael
448 (1991) to shift the Fe^{3+}/Fe^{2+} ratio in the same direction, whereas Moretti (2005) suggests
449 an insignificant change. It is difficult to clearly attribute the observed shift in Fe^{3+}/Fe^{2+} to
450 either K_2O or ΣFeO. A stabilization of tetrahedrally coordinated ferric iron by charge-
451 balancing K_2O has been suggested by various authors (Sack et al., 1980; Kilinc et al.,
452 1983; Dickenson and Hess, 1986; Kress and Carmichael, 1988) supporting that K_2O has a
453 positive impact on the ferric-ferrous ratio.
454 Noteworthy, in contrast to the model predictions and our findings, Tangeman et
455 al. (2001) proposed a negative effect of increasing K_2O and a positive effect of increasing
456 ΣFeO on the Fe^{3+}/Fe^{2+} ratio. However, these discrepancies may be due to significant

457 compositional differences, since these authors investigated anhydrous K_2O-FeO-Fe_2O_3-
458 SiO_2 liquids and their experiments were performed at atmospheric pressure.
459
460 **Effect of temperature and pressure on the redox state of iron**

461 The models of Kress and Carmichael (1991) and Moretti (2005) both predict a
462 small positive dependence of the $Fe^{2+}/\Sigma Fe$ ratio on temperature. At a given f_{O_2}, both
463 models calculate an increase of the $Fe^{2+}/\Sigma Fe$ ratio by 0.01 to 0.08 when the temperature is
464 raised from 1200 to 1250°C. This effect is more pronounced at lower pressure and higher
465 oxygen fugacity. The comparison of our experimental datasets obtained at 1200°C and
466 1250°C reveals no clearly resolvable systematic trend regarding experimental and
467 analytical uncertainties. However, predicted effects on the iron redox state caused by this
468 moderate temperature change are small and therefore difficult to resolve.

469 To evaluate the effect of pressure on the redox state of iron we performed
470 experiments at pressures from 50 to 500 MPa (Table 1) at intrinsic redox conditions in
471 the IHPV (NNO+2.6). All experiments were done with a pure H_2O fluid to obtain a water
472 saturated silicate melt. In Figure 7a, the $Fe^{2+}/\Sigma Fe$ ratios of the silicate glasses are shown
473 as a function of pressure. The data suggest a slight negative trend with increasing
474 pressure. However, this trend is basically defined by the 50 MPa experiments, whereas
475 most of the experimentally obtained $Fe^{2+}/\Sigma Fe$ ratios agree within uncertainties.
476 Furthermore, it is important to note that the water solubility in the melt increases with
477 increasing pressure (Fig. 7b) and hence for a comparison of the experiments a
478 superimposed effect of water content – as suggested by Moretti (2005) – has to be
479 considered as well.

Both models (Kress and Carmichael, 1991; Moretti, 2005) predict a nonlinear positive dependence of the $Fe^{2+}/\Sigma Fe$ ratio on increasing pressure (Fig. 7a). According to the model of Moretti (2005) the pressure effect is more prominent for water-rich than for dry melts. Our experiments at $a_{H_2O} = 1$ cover a range from about 2.4 to 12 wt% H_2O and the measured $Fe^{2+}/\Sigma Fe$ ratios are consistent with the range of $Fe^{2+}/\Sigma Fe$ calculated by the model of Moretti (2005) for corresponding water contents. Thus, the dependence of the Fe redox state on water contents (linked to the specific pressures) that is superimposed on the pressure effect could explain the seeming negative trend mentioned above. No analytically resolvable change in the Fe redox ratio is found within the pressure range investigated in this study. An extension of the experimental dataset to higher pressures is needed to better constrain the effect of pressure on $Fe^{2+}/\Sigma Fe$ in hydrous silicate melts and to allow a comparison to anhydrous silicate melts, e.g. O'Neill et al. (2006), where a pressure effect was observed. Such data are useful to retrieve precise information about partial molar volumes of iron species for thermodynamic modeling.

CONCLUDING REMARKS

An experimental study was performed to investigate the dependence of the $Fe^{2+}/\Sigma Fe$ ratio in phono-tephritic melts on oxygen fugacity. The redox conditions were adjusted at prevailing f_{H_2} using mixed H_2O-CO_2 fluids which control the water activity in the system. The experimentally obtained relationship between f_{O_2} and Fe^{3+}/Fe^{2+} for hydrous ultrapotassic melts is in general agreement with predictions from the models of Kress and Carmichael (1991) and Moretti (2005). This suggests that these models can be

applied to phono-tephritic melts as well, although such compositions were not implemented in the model calibrations.

A small negative effect of dissolved water on $Fe^{2+}/\Sigma Fe$ at given f_{O_2} was found that confirms the predictions of the thermodynamic model of Moretti (2005). On the other hand, no effect of pressure and temperature on the redox state of iron was resolvable in the investigated P-T range. Compared to hydrous ferrobasaltic melts systematically higher $Fe^{2+}/\Sigma Fe$ ratios were found for the phono-tephrite in particular at low oxygen fugacity. This effect is most likely due to the much higher K_2O contents of the phono-tephrite (7.5 wt% compared to 0.3 wt%). However, the difference in ΣFeO (7.8 wt% in the phono-tephrite and 12.9 wt% in the ferrobasalt) may additionally contribute to the observed differences in $Fe^{2+}/\Sigma Fe$. The new data may be used to improve the computation models, i.e., to calibrate the effects of H_2O, K_2O and FeO on the redox state or iron in silicate melts. Furthermore, complementing other recent investigations (e.g., Freda et al., 2006; Gaeta et al., 2006; Carapezza and Tarchini, 2007; Freda et al., in press), this study contributes to a better understanding of the redox conditions of the Alban hills magmatic system and of potassic magmatism, in general.

ACKNOWLEDGEMENTS

Thanks to Francesco Vetere, Renat Almeev and Sara Fanara, Henrike Baumgarten for their help with the experiments and KFT measurements, respectively. All experiments and analytical determinations were performed at the Institute of Mineralogy of the Leibniz University of Hannover, Germany. We would like to express our thanks to Claudia Thuernagel and Anna Wegorzewski for their support during the Fe redox analysis. Thanks to Christian Bertoldi for

generously providing the chlorite sample CA. Otto Diedrich is acknowledged for preparation of the thin sections. We thank the reviewers Mathieu Roskosz and Roberto Moretti for their helpful comments and AE Grant Henderson is acknowledged for efficient editorial handling. This research was supported by DFG grants SCHO-1071/1-1&2, INGV-DPC Project V3_1 Colli Albani and by Project FIRB MIUR "Development of innovative technologies for the environmental protection from natural events".

APPENDIX 1 - Reagents used for wet-chemical colorimetric iron determination

All reagents were freshly prepared before each analytical session:

Ammonium vanadate solution. 0.165 g NH_4VO_3 (Alfa Aesar, 99.93% metals basis) were dissolved in 100 mL distilled water and H_2SO_4 (Merck, p.a.). The final concentration of H_2SO_4 was generally 1*M*, or in some cases up to 5*M* to test whether the sulphuric acid concentration has an influence on the ferrous iron determination (see text). 1 mL of this solution was added to each sample (corresponds to ~14.1 µmol NH_4VO_3), capable to oxidize about 800 µg ferrous Fe. We always processed <500 µg Fe to ensure V^{5+} excess.

Boric acid solution. Approximately 20 g H_3BO_3 (Merck, p.a.) were dissolved in ~100 mL distilled water at ~80°C to obtain a saturated solution. After sample dissolution 5 mL of the hot solution was added to each sample.

2:2'bipyridyl solution. 0.15 g $C_{10}H_8N_2$ (Alfa Aesar, p.a.) were dissolved in 100 mL distilled water. 5 mL of this solution (corresponds to ~9.6 µmol $C_{10}H_8N_2$) was added to each sample. This amount can complex about 900 µg ferrous Fe to form the colored chromophore. Less than <500 µg Fe were processed to ensure 2:2'bipyridyl excess.

550 *Ammonium acetate solution***:** Approximately 20 g CH_3COONH_4 were dissolved in 200
551 mL distilled water.
552 *Hydroxylamine hydrochloride*. Between 5 and 10 mg $NH_2OH{\cdot}HCl$ (Merck, p.a.) were
553 added to each 10-mL-sample-aliquot containing <50 µg ferric Fe, to ensure quantitative
554 reduction. At least 8 mg ferric Fe can be reduced by this amount (>72 µmol
555 $NH_2OH{\cdot}HCl$).
556 *Hydrofluoric acid* was 24% or 48% (v/v, Merck, p.a.) (see text).
557 *Ferrous ammonium sulphate.* $(NH_4)_2Fe(SO_4)_2 \cdot 6H_2O$ (Merck, p.a.). Standards with
558 concentrations between 1 and 8 µg/mL ferrous Fe were prepared in 1*M* H_2SO_4 for
559 quantitative calibration of the method.
560
561

562 **REFERENCES CITED**

563 Aranovich, L.Y., and Newton, R.C. (1999) Experimental determination of CO_2-H_2O
564 activity-composition relations at 600-1000 degrees C and 6-14 kbar by reversed
565 decarbonation and dehydration reactions. American Mineralogist, 84(9), 1319-
566 1332.

567 Baker, L.L., and Rutherford, M.J. (1996) The effect of dissolved water on the oxidation
568 state of silicic melts. Geochimica et Cosmochimica Acta, 60(12), 2179-2187.

569 Behrens, H., Zhang, Y.X., and Xu, Z.G. (2004) H_2O diffusion in dacitic and andesitic
570 melts. Geochimica et Cosmochimica Acta, 68(24), 5139-5150.

571 Berndt, J., Liebske, C., Holtz, F., Freise, M., Nowak, M., Ziegenbein, D., Hurkuck, W.,
572 and Koepke, J. (2002) A combined rapid-quench and H_2-membrane setup for
573 internally heated pressure vessels: Description and application for water solubility
574 in basaltic melts. American Mineralogist, 87, 1717-1726.

575 Bertoldi, C., Dachs, E., and Appel, P. (2007) Heat-pulse calorimetry measurements on
576 natural chlorite-group minerals. American Mineralogist, 92(4), 553-559.

Borisov, A.A., and Shapkin, A.I. (1989) New empiric equation of dependence of Fe^{3+}/Fe^{2+} ratio in natural Melts on their composition, oxygen fugacity and temperature. Geokhimiya (6), 892-897.

Botcharnikov, R.E., Behrens, H., and Holtz, F. (2006) Solubility and speciation of C-O-H fluids in andesitic melt at T = 1100-1300 °C and P = 200 and 500 MPa. Chemical Geology, 229(1-3), 125-143.

Botcharnikov, R.E., Koepke, J., Holtz, F., McCammon, C., and Wilke, M. (2005) The effect of water activity on the oxidation and structural state of Fe in a ferro-basaltic melt. Geochimica et Cosmochimica Acta, 69(21), 5071-5085.

Burgisser, A., and Scaillet, B. (2007) Redox evolution of a degassing magma rising to the surface. Nature, 445(7124), 194-197.

Carapezza, M.L., and Tarchini, L. (2007) Accidental gas emission from shallow pressurized aquifers at Alban Hills volcano (Rome, Italy): Geochemical evidence of magmatic degassing? Journal of Volcanology and Geothermal Research, 165(1-2), 5-16.

Carmichael, I.S.E. (1991) The redox states of basic and silicic magmas - a reflection of their source regions. Contributions to Mineralogy and Petrology, 106(2), 129-141.

Chou, I.M. (1986) Permeability of precious metals to hydrogen at 2 kbar total pressure and elevated temperatures. American Journal of Science, 286, 638-658.

Dickenson, M.P., and Hess, P.C. (1986) The structural role and homogeneous redox equilibria of iron in peraluminous, metaluminous and peralkaline silicate melts. Contributions to Mineralogy and Petrology, 92(2), 207-217.

Freda, C., Gaeta, M., Karner, D.B., Marra, F., Renne, P.R., Taddeucci, J., Scarlato, P., Christensen, J.N., and Dallai, L. (2006) Eruptive history and petrologic evolution of the Albano multiple maar (Alban Hills, Central Italy). Bulletin of Volcanology, 68(6), 567-591.

Freda, C, Gaeta, M., Misiti, V., Mollo, S., Dolfi, D., Scarlato, P. (in press) Magma-carbonate interaction: an experimental study on ultrapotassic rocks from Alban Hills (Central Italy). Lithos. doi 10.1016/j.lithos.2007.08.008

Gaeta, M., Freda, C., Christensen, J.N., Dallai, L., Marra, F., Karner, D.B., and Scarlato, P. (2006) Time-dependent geochemistry of clinopyroxene from the Alban Hills (Central Italy): Clues to the source and evolution of ultrapotassic magmas. Lithos, 86(3-4), 330-346.

Gaillard, F., Pichavant, M., and Scaillet, B. (2003) Experimental determination of activities of FeO and Fe_2O_3 components in hydrous silicic melts under oxidizing conditions. Geochimica et Cosmochimica Acta, 67(22), 4389-4409.

618 Gaillard, F., Scaillet, B., and Pichavant, M. (2002) Kinetics of iron oxidation-reduction in
619 hydrous silicic melts. American Mineralogist, 87(7), 829-837.

620 Gaillard, F., Scaillet, B., Pichavant, M., and Beny, J.L. (2001) The effect of water and
621 fO(2) on the ferric-ferrous ratio of silicic melts. Chemical Geology, 174(1-3),
622 255-273.

623 Govindaraju, K. (1994) 1994 compilation of working values and sample description for
624 383 geostandards. Geostandards Newsletter, 18, 1-158.

625 Govindaraju, K. (1995) 1995 working values with confidence-limits for 26 CRPG,
626 ANRT and IWG-GIT geostandards. Geostandards Newsletter, 19, 1-33.

627 Holloway, J.R., and Blank, J.G. (1994) Application of experimental results to C-O-H
628 species in natural melts. In M.R. Carroll, and J.R. Holloway, Eds. Volatiles in
629 magmas, 30, p. 187-230. Mineralogical Society of America, Washington, DC,
630 United States.

631 Huebner, J.S., and Sato, M. (1970) The oxygen fugacity-temperature relationships of
632 manganese and nickel oxide buffers. American Mineralogist, 55, 934-952.

633 Jayasuriya, K.D., O'Neill, H.S., Berry, A.J., and Campbell, S.J. (2004) A Mossbauer
634 study of the oxidation state of Fe in silicate melts. American Mineralogist, 89(11-
635 12), 1597-1609.

636 Kilinc, A., Carmichael, I.S.E., Rivers, M.L., and Sack, R.O. (1983) The ferric-ferrous
637 ratio of natural silicate liquids equilibrated in air. Contributions to Mineralogy and
638 Petrology, 83(1-2), 136-140.

639 Kress, V.C., and Carmichael, I.S.E. (1988) Stoichiometry of the iron oxidation reaction in
640 silicate melts. American Mineralogist, 73(11-12), 1267-1274.

641 Kress, V.C., and Carmichael, S.E. (1991) The compressibility of silicate liquidus
642 containing Fe_2O_3 and the effect of composition, temperature, oxygen fugacity and
643 pressure on their redox states. Contributions to Mineralogy and Petrology, 108, p.
644 82-92.

645 Liebske, C., Behrens, H., Holtz, F., and Lange, R.A. (2003) The influence of pressure and
646 composition on the viscosity of andesitic melts. Geochimica et Cosmochimica
647 Acta, 67(3), 473-485.

648 Marra, F., Freda, C., Scarlato, P., Taddeucci, J., Karner, D.B., Renne, P.R., Gaeta, M.,
649 Palladino, D.M., Trigila, R., and Cavarretta, G. (2003) Post-caldera activity in the
650 Alban Hills volcanic district (Italy): Ar-40/Ar-39 geochronology and insights into
651 magma evolution. Bulletin of Volcanology, 65(4), 227-247.

652 Misiti, V., Behrens, H., Freda, C., Vetere, F., Botcharnikov, R.E. and Scarlato, P. (this
653 issue) Solubility of H_2O and CO_2 in potassic melts at 1200 and 1250 °C and
654 pressure from 50 to 500 MPa. American Mineralogist.

655 Moore, G., Righter, K., and Carmichael, I.S.E. (1995) The effect of dissolved water on
656 the oxidation-state of iron in natural silicate liquids. Contributions to Mineralogy
657 and Petrology, 120(2), 170-179.

658 Moretti, R. (2005) Polymerisation, basicity, oxidation state and their role in ionic
659 modelling of silicate melts. Annals of Geophysics, 48(4-5), 583-608.

660 Moretti, R., and Ottonello, G. (2003) Polymerization and disproportionation of iron and
661 sulfur in silicate melts: insights from an optical basicity-based approach. Journal
662 of Non-Crystalline Solids, 323(1-3), 111-119.
663
664 Moretti, R., and Papale, P. (2004) On the oxidation state and volatile behavior in
665 multicomponent gas-melt equilibria. Chemical Geology, 213(1-3), 265-280.
666
667 Mysen, B.O. (1988) Structure and Properties of Silicate Melts. 354 p., Elsevier,
668 Amsterdam.

669 Nikolaev, G.S., Borisov, A.A., and Ariskin, A.A. (1996) Calculation of the ferric-ferrous
670 ratio in magmatic melts: Testing and additional calibration of empirical equations
671 for various magmatic series. Geokhimiya(8), 713-722.

672 O'Neill, H.S.C., Berry, A.J., McCammon, C.C., Jayasuriya, K.D., Campbell, S.J., and
673 Foran, G. (2006) An experimental determination of the effect of pressure on the
674 $Fe^{3+}/\Sigma Fe$ ratio of an anhydrous silicate melt to 3.0 GPa. American Mineralogist,
675 91(2-3), 404-412.

676 Ottonello, G., Moretti, R., Marini, L., and Zuccolini, M.V. (2001) Oxidation state of iron
677 in silicate glasses and melts: a thermochemical model. Chemical Geology, 174(1-
678 3), 157-179.

679 Partzsch, G.M., Lattard, D., and McCammon, C. (2004) Mossbauer spectroscopic
680 determination of Fe^{3+}/Fe^{2+} in synthetic basaltic glass: a test of empirical fO_2
681 equations under superliquidus and subliquidus conditions. Contributions to
682 Mineralogy and Petrology, 147(5), 565-580.

683 Pichavant, M., Martel, C., Bourdier, J.L., and Scaillet, B. (2002) Physical conditions,
684 structure, and dynamics of a zoned magma chamber: Mount Pelee (Martinique,
685 Lesser Antilles Arc). Journal of Geophysical Research - Solid Earth, 107(B5), 1-
686 28.
687

688 Pitzer, K.S., and Sterner, S.M. (1994) Equation of state valid continuously from zero to
689 extreme pressures for H_2O and CO_2. Journal of Chemical Physics, 102, 3111-
690 3116.

691 Pouchou, J.L., and Pichoir, F. (1991) Quantitative analysis of homogeneous or stratified
692 microvolumes applying the model ‘‘PAP’’. In K.F.J. Heinrich, and D.E.
693 Newbury, Eds. Electron probe quantitation, p. 31-75. Plenum Press, New York.

694 Robie, R.A., Hemingway, B.S., and Fischer, J.R. (1978) Thermodynamic properties of
695 minerals and related substances at 298.15 K and 1 bar (105 Pascals) pressure and
696 at higher temperature. Geological Survey Bulletin, 1452, 456.

697 Sack, R.O., Carmichael, I.S.E., Rivers, M., and Ghiorso, M.S. (1980) Ferric-Ferrous
698 Equilibria in Natural Silicate Liquids at 1bar. Contributions to Mineralogy and
699 Petrology, 75(4), 369-376.

700 Sisson, T.W., and Grove, T.L. (1993) Experimental investigations of the role of H_2O in
701 calc-alkaline differentiation and subduction zone magmatism. Contributions to
702 Mineralogy and Petrology, 113(2), 143-166.

703 Tangeman, J.A., Lange, R., and Forman, L. (2001) Ferric-ferrous equilibria in K_2O-FeO-
704 Fe_2O_3-SiO_2 melts. Geochimica et Cosmochimica Acta, 65(11), 1809-1819.

705 Taylor, J.R., Wall, V.J., and Pownceby, M.I. (1992) The calibration and application of
706 accurate redox sensors. American Mineralogist, 77, p. 284-295.

707 Vetere, F., Behrens, H., Holtz, F., and Neuville, D.R. (2006) Viscosity of andesitic melts
708 - new experimental data and a revised calculation model. Chemical Geology,
709 228(4), 233-245.
710
711 Watson, E.B., and Baxter, E.F. (2007) Diffusion in solid-Earth systems. Earth and
712 Planetary Science Letters, 253(3-4), 307-327.

713 Whipple, E.R. (1974) Study of Wilsons determination of ferrous iron in silicates.
714 Chemical Geology, 14(3), 223-238.

715 Wilke, M., Behrens, H., Burkhard, D.J.M., and Rossano, S. (2002) The oxidation state of
716 iron in silicic melt at 500 MPa water pressure. Chemical Geology, 189(1-2), 55-
717 67.

718 Wilson, A.D. (1960) The micro-determination of ferrousiron in silicate minerals by a
719 volumetric and colorimetric method. Analyst, 85, 823-827.

720 Yokoyama, T., and Nakamura, E. (2002) Precise determination of ferrous iron in silicate
721 rocks. Geochimica et Cosmochimica Acta, 66(6), 1085-1093.
722
723

724
725

Table 1. Summary of experimental conditions, results of wet-chemical colorimetric iron analyses and $Fe^{2+}/\Sigma Fe$ ratios from model calculations after Moretti (2005) and Kress and Carmichael (1991).

	experimental conditions								wet-chemical colorimetric analyses							model calculations	
sample	run[a]	P	T	t	$X^{f}_{H_2O}$ [b]	a_{H_2O} [c]	$\log f_{O_2}$ [d]	ΔNNO[e]	sample weight	A_{523} Fe^{2+}	A_{523} ΣFe	ΣFeO		$Fe^{2+}/\Sigma Fe$		$Fe^{2+}/\Sigma Fe$	
		(MPa)	(°C)	(h)					(mg)			(wt%)	(2σ)		(2σ)	(Moretti)	(K&C)
Ar-IHPV (f_{H_2} intrinsic); H_2O fluid, a_{H_2O} = 1																	
Alb1-20	A	50	1250	15	1.00	1.00	-4.39	2.60	4.65	0.2323	0.3880	7.07	0.24	0.60	0.02	0.40	0.48
									6.01	0.2999	0.5014	7.06	0.22	0.60	0.02	0.40	0.48
Alb1-21	A	50	1250	15	1.00	1.00	-4.39	2.60	5.76	0.2886	0.4852	7.12	0.22	0.59	0.02	0.39	0.48
Alb1-22	B	100	1250	20	1.00	1.00	-4.38	2.60	4.54	0.1953	0.3921	7.31	0.25	0.50	0.02	0.39	0.48
Alb1-23	B	100	1250	20	1.00	1.00	-4.38	2.60	4.57	0.1877	0.3775	6.99	0.24	0.50	0.02	0.39	0.48
Alb1-36	C	200	1200	20	1.00	1.00	-4.90	2.60	5.64	0.2307	0.4665	7.00	0.22	0.49	0.02	0.41	0.48
Alb1-37	C	200	1200	20	1.00	1.00	-4.90	2.60	3.50	0.1607	0.2994	7.25	0.28	0.54	0.03	0.42	0.48
Alb1-10	D	200	1250	20	1.00	1.00	-4.35	2.60	5.89	0.2176	0.4986	7.17	0.22	0.44	0.02	0.41	0.49
Alb1-24[e]	E	300	1250	14	1.00	1.00	-4.32	2.60	4.78	0.1877	0.3918	6.94	0.23	0.48	0.02	0.43	0.49
Alb1-25[e]	E	300	1250	14	1.00	1.00	-4.32	2.60	4.79	0.1870	0.3922	6.93	0.23	0.48	0.02	0.43	0.49
Alb1-35[e]	F	400	1200	72	1.00	1.00	-4.84	2.60	5.53	0.2148	0.4477	6.85	0.22	0.48	0.02	0.45	0.50
Alb1-26[e]	G	400	1250	48	1.00	1.00	-4.29	2.60	4.69	0.1848	0.3772	6.81	0.23	0.49	0.02	0.45	0.50
Alb1-27[e]	G	400	1250	48	1.00	1.00	-4.29	2.60	4.58	0.1764	0.3630	6.72	0.23	0.49	0.02	0.45	0.50
Alb1-5[e]	H	500	1200	20	1.00	1.00	-4.81	2.60	4.12	0.1500	0.3298	6.78	0.25	0.45	0.03	0.46	0.50
Alb1-15[e]	I	500	1250	20	1.00	1.00	-4.26	2.60	4.55	0.1544	0.3759	6.99	0.24	0.41	0.02	0.48	0.51
									4.98	0.1619	0.3934	6.69	0.22	0.41	0.02	0.48	0.51
Alb1-28[e]	L	500	1250	17	1.00	1.00	-4.26	2.60	1.95	0.0723	0.1579	6.84	0.40	0.46	0.06	0.47	0.51
Alb1-41	N	200	1200	24	1.00	1.00	-4.90	2.60	5.49	0.2366	0.4641	7.16	0.23	0.51	0.02	0.44	0.48
Ar-IHPV (f_{H_2} intrinsic); H_2O-CO_2 fluid																	
Alb1-7	D	200	1250	18	0.33	0.40	-5.15	1.80	4.46	0.2322	0.3805	7.23	0.25	0.61	0.02	0.58	0.58
Alb1-8	D	200	1250	18	0.50	0.57	-4.84	2.10	4.49	0.2183	0.3946	7.44	0.25	0.55	0.02	0.52	0.55
Alb1-6bis	M	200	1250	20	0.10	0.13	-6.10	0.85	4.52	0.2555	0.3277	6.13	0.22	0.78	0.03	0.75	0.67
Alb1-6a	M	200	1250	20	0.18	0.23	-5.62	1.33	4.97	0.2649	0.3822	6.51	0.22	0.69	0.03	0.68	0.63
Alb1-1[e]	H	500	1200	18	n.a.	0.15[e]	-6.47	0.93	4.45	0.2658	0.3187	6.07	0.22	0.83	0.03	0.78	0.68
Alb1-2	H	500	1200	18	0.22	0.28	-5.91	1.50	3.99	0.2191	0.3425	7.27	0.26	0.64	0.03	0.69	0.63
Alb1-3	H	500	1200	18	0.60	0.66	-5.17	2.23	4.56	0.1952	0.3653	6.78	0.23	0.53	0.02	0.56	0.55
									2.45	0.1013	0.2005	6.92	0.34	0.51	0.04	0.56	0.55
Alb1-4[e]	H	500	1200	18	0.83	0.85	-4.95	2.46	4.18	0.1617	0.3537	7.17	0.25	0.46	0.02	0.50	0.46
Alb1-12	I	500	1250	18	0.32	0.39	-5.08	1.78	4.62	0.2167	0.4055	7.42	0.25	0.53	0.02	0.63	0.54
Alb1-13[e]	I	500	1250	18	0.75	0.78	-4.47	2.38	3.55	0.1368	0.3052	7.27	0.27	0.45	0.03	0.51	0.47
Alb1-14[e]	I	500	1250	18	0.79	0.81	-4.44	2.42	4.48	0.1714	0.3870	7.32	0.25	0.44	0.02	0.51	0.47

continued on next page

726
727

Table 1. - continued

sample	run[a]	P (MPa)	T (°C)	t (h)	$X^{f}_{H_2O}$ [b]	a_{H_2O} [c]	log f_{O_2} [d]	ΔNNO[e]	sample weight (mg)	A_{523} Fe^{2+}	A_{523} ΣFe	ΣFeO (wt%)	(2σ)	Fe^{2+}/ΣFe	(2σ)	Fe^{2+}/ΣFe (Moretti)	Fe^{2+}/ΣFe (K&C)
		experimental conditions							wet-chemical colorimetric analyses							model calculations	
Ar-H_2-IHPV (f_{H_2} varied); H_2O fluid or H_2O-CO_2 fluid																	
Alb1-H42	O	200	1200	18	1.00	1.00	-5.64	1.87	5.56	0.2302	0.4640	7.06	0.22	0.50	0.02	0.51	0.57
Alb1-H43	O	200	1200	18	0.76	0.78	-5.86	1.65	5.48	0.2357	0.4611	7.12	0.23	0.51	0.02	0.55	0.53
Alb1-H44	O	200	1200	18	0.30	0.34	-6.57	0.93	5.59	0.2863	0.4658	7.05	0.22	0.61	0.02	0.69	0.61
									4.47	0.2251	0.3705	7.02	0.24	0.61	0.03	0.69	0.61
Alb1-H45	O	200	1200	18	0.07	0.09	-7.78	-0.28	5.27	0.2921	0.4083	6.55	0.22	0.72	0.02	0.84	0.73
									4.37	0.2379	0.3359	6.50	0.23	0.71	0.03	0.84	0.73
Alb1-H47	P	200	1200	5	1.00	1.00	-7.70	-0.20	5.11	0.2883	0.3646	6.04	0.21	0.79	0.03	0.77	0.76
Alb1-H48	P	200	1200	5	0.71	0.73	-7.97	-0.47	5.20	0.3039	0.3893	6.34	0.21	0.78	0.03	0.81	0.74
Alb1-H49	P	200	1200	5	0.39	0.43	-8.43	-0.93	5.70	0.3057	0.3720	5.52	0.19	0.82	0.03	0.87	0.78
Alb1-H50	P	200	1200	5	0.23	0.27	-8.85	-1.35	5.02	0.2371	0.2886	4.87	0.19	0.82	0.04	0.90	0.81
									4.07	0.1949	0.2338	4.86	0.21	0.83	0.04	0.90	0.81
Alb1-H51	P	200	1200	5	0.14	0.17	-9.26	-1.76	5.36	0.2084	0.2577	4.07	0.17	0.81	0.04	0.93	0.83
									3.82	0.1594	0.1976	4.37	0.21	0.81	0.05	0.93	0.86
Alb1-H52	Q	200	1200	1.5	1.00	1.00	-7.80	-0.29	5.26	0.3419	0.4567	7.34	0.23	0.75	0.02	0.79	0.72
Alb1-H54	Q	200	1200	1.5	0.50	0.53	-8.35	-0.85	6.24	0.4169	0.5276	7.16	0.22	0.79	0.02	0.86	0.76
Alb1-H56	Q	200	1200	1.5	0.04[f]	0.05	-10.40[f]	-2.90[f]	5.23	0.2842	0.3342	5.41	0.19	0.85	0.03	0.96	0.89

n.a. not available

a) Each letter refers to an individual run in the IHPV, containing one or more samples, i.e. capsules.

b) Mole fraction of water and CO_2 in the fluid phase measured by the weight loss method (see text).

c) Water activities for mixed H_2O-CO_2 fluids were calculated from $X^{f}H_2O$ after Aranovich and Newton (1999) using molar volumes of pure H_2O and CO_2 from Pitzer and Sterner (1994).

d) Oxygen fugacity calculated from water activity: $\log fO_2 = \log fO_2(IHPV_{apparent}) + 2\log(aH_2O)$, where $fO_2(IHPV_{apparent})$ is the oxygen fugacity in the capsule at $aH_2O = 1$ imposed by the fH_2 in the IHPV (intrinsic of defined by Ar-H_2 mixtures). ΔNNO is $\log fO_2$ expressed relative to the Ni-NiO buffer.

e) Experimental products which contain quench crystals formed during cooling at the end of the experiment. All other run products consist of glass and a fluid phase only; except sample Alb1-1, which additionally contains clinopyroxene crystals formed in equilibrium with the silicate melt at experimental conditions (see text).

f) Fluid composition in mole fractions ($X^{f}H_2O$, $X^{f}CO_2$, $X^{f}CO$) for sample Alb1-H56 (that was used to calculate the oxygen fugacity) estimated from CO_2 solubility trends due to presence of other carbon species (beside CO_2) in the fluid (see text).

g) Water activity was calculated from an estimated $X^{f}H_2O$ of 0.11 for Alb1-1 (see text).

Notes for wet-chemical colorimetric analyses: A_{523} values are the measured baseline-corrected absorbances at the Fe(II)-2'2-bipyridiyl absorbance maximum at about 523 nm. Given uncertainties calculated from error propagation of individual uncertainties in sample weight, dilution and absorbance measurements. The external reproducibility (2σ) of the $Fe^{2+}/\Sigma Fe$ ratio with this method is 0.03 (see text). Multiple analyses for the same sample represent full wet-chemical replicates including individual dissolution of fragments from the experimental products.

728
729

Table 2. Electron microprobe analyses of the starting phono-tephritic glass and the experimental glasses. Analysis of the ferrobasalt SC1 studied by Botcharnikov et al. (2005) is shown for comparison, to highlight compositional differences. Given are averages and the standard deviation s(1σ) of n replicate analyses reported in wt%.

sample	n	SiO_2	Al_2O_3	ΣFeO	MgO	CaO	MnO	TiO_2	Na_2O	K_2O	Total	ΣFeO norm[b]
phono-tephritic starting glass												
Alb1	31	49.89 ± 0.42	15.57 ± 0.21	7.82 ± 0.32	5.75 ± 0.18	11.40 ± 0.21	0.02 ± 0.09	0.89 ± 0.03	1.95 ± 0.18	7.52 ± 0.16	100.80 ± 0.67	7.75
ferrobasalt from Botcharnikov et. al (2005)												
SC1		48.34 ± 0.29	14.61 ± 0.13	12.91 ± 0.28	6.40 ± 0.11	10.87 ± 0.15	-	2.86 ± 0.05	2.60 ± 0.11	0.30 ± 0.03	98.89 ± 0.67	13.05
experimental products												
Alb1-1	8	48.31 ± 0.40	15.65 ± 0.26	6.09 ± 0.32	5.22 ± 0.17	10.53 ± 0.19	0.04 ± 0.08	0.91 ± 0.06	2.14 ± 0.12	7.47 ± 0.08	96.36 ± 0.83	6.32
Alb1-2	11	46.20 ± 0.27	14.56 ± 0.14	6.92 ± 0.22	5.31 ± 0.10	10.44 ± 0.24	0.01 ± 0.06	0.83 ± 0.06	1.97 ± 0.12	6.90 ± 0.14	93.14 ± 0.62	7.43
Alb1-5[a]	9	44.42 ± 0.68	13.94 ± 0.16	6.58 ± 0.73	4.93 ± 0.81	10.28 ± 1.56	0.05 ± 0.08	0.80 ± 0.04	1.78 ± 0.19	6.56 ± 0.53	89.35 ± 0.81	7.37
Alb1-8	11	46.82 ± 0.38	14.61 ± 0.18	7.01 ± 0.22	5.26 ± 0.11	10.38 ± 0.22	0.08 ± 0.08	0.83 ± 0.03	1.94 ± 0.12	7.04 ± 0.15	93.96 ± 0.67	7.46
Alb1-6a	11	48.08 ± 0.35	15.08 ± 0.16	6.74 ± 0.36	5.40 ± 0.10	10.91 ± 0.26	0.01 ± 0.08	0.87 ± 0.05	2.02 ± 0.09	7.14 ± 0.14	96.27 ± 0.63	7.00
Alb1-6bis	11	48.54 ± 0.49	15.29 ± 0.18	5.95 ± 0.26	5.50 ± 0.15	10.92 ± 0.25	0.03 ± 0.10	0.91 ± 0.04	2.06 ± 0.24	7.33 ± 0.11	96.55 ± 0.95	6.16
Alb1-14	11	44.56 ± 0.39	13.98 ± 0.16	6.77 ± 0.30	4.94 ± 0.19	9.96 ± 0.20	0.02 ± 0.05	0.79 ± 0.04	1.82 ± 0.10	6.74 ± 0.12	89.58 ± 0.61	7.56
Alb1-20	12	47.28 ± 0.49	14.83 ± 0.24	6.94 ± 0.23	5.44 ± 0.20	10.66 ± 0.26	0.01 ± 0.07	0.86 ± 0.02	2.01 ± 0.11	7.10 ± 0.14	95.14 ± 0.86	7.30
Alb1-23	12	47.06 ± 0.38	14.65 ± 0.15	7.04 ± 0.29	5.20 ± 0.11	10.49 ± 0.25	0.06 ± 0.06	0.84 ± 0.04	1.97 ± 0.11	6.93 ± 0.13	94.24 ± 0.54	7.47
Alb1-25	12	45.47 ± 0.35	14.06 ± 0.13	6.79 ± 0.22	5.00 ± 0.08	9.99 ± 0.16	0.06 ± 0.08	0.82 ± 0.03	1.81 ± 0.16	6.72 ± 0.16	90.73 ± 0.38	7.48
Alb1-26	12	44.77 ± 0.27	14.03 ± 0.19	6.69 ± 0.29	5.14 ± 0.16	9.89 ± 0.27	0.05 ± 0.07	0.79 ± 0.03	1.80 ± 0.14	6.62 ± 0.12	89.78 ± 0.61	7.45
Alb1-41	12	46.42 ± 0.41	14.56 ± 0.25	7.06 ± 0.33	5.27 ± 0.16	10.70 ± 0.24	0.01 ± 0.08	0.83 ± 0.04	1.81 ± 0.08	7.12 ± 0.13	93.78 ± 0.69	7.53
Alb1-H42	15	45.57 ± 0.35	14.18 ± 0.21	6.85 ± 0.25	5.03 ± 0.13	10.32 ± 0.28	0.02 ± 0.10	0.83 ± 0.03	1.77 ± 0.13	7.06 ± 0.11	91.63 ± 0.58	7.48
Alb1-H43	18	45.28 ± 0.35	14.22 ± 0.18	7.03 ± 0.33	5.21 ± 0.15	10.34 ± 0.27	0.06 ± 0.06	0.83 ± 0.05	1.87 ± 0.12	7.04 ± 0.15	91.86 ± 0.75	7.65
Alb1-H44	13	46.69 ± 0.41	14.63 ± 0.20	6.91 ± 0.39	5.36 ± 0.13	10.75 ± 0.21	0.01 ± 0.05	0.87 ± 0.06	1.91 ± 0.15	7.18 ± 0.17	94.30 ± 0.72	7.33
Alb1-H45	16	47.39 ± 0.83	14.98 ± 0.23	6.32 ± 0.35	5.29 ± 0.28	10.78 ± 0.31	0.03 ± 0.06	0.87 ± 0.05	1.87 ± 0.14	7.42 ± 0.19	94.94 ± 1.39	6.65
Alb1-H47	12	45.60 ± 0.27	14.18 ± 0.24	6.17 ± 0.24	5.14 ± 0.18	10.46 ± 0.24	0.03 ± 0.08	0.87 ± 0.02	1.79 ± 0.14	7.10 ± 0.12	91.33 ± 0.65	6.75
Alb1-H48	14	46.24 ± 0.45	14.46 ± 0.16	6.40 ± 0.16	5.23 ± 0.11	10.37 ± 0.19	0.01 ± 0.07	0.84 ± 0.03	1.90 ± 0.22	7.13 ± 0.15	92.58 ± 0.47	6.92
Alb1-H49	16	46.97 ± 0.56	14.80 ± 0.24	5.52 ± 0.35	5.32 ± 0.16	10.64 ± 0.29	0.03 ± 0.07	0.86 ± 0.04	1.87 ± 0.15	7.37 ± 0.16	93.39 ± 0.71	5.91
Alb1-H50	16	48.01 ± 0.39	15.13 ± 0.21	4.72 ± 0.32	5.41 ± 0.15	10.83 ± 0.18	0.02 ± 0.06	0.85 ± 0.04	1.95 ± 0.15	7.56 ± 0.17	94.47 ± 0.59	5.00
Alb1-H51	20	47.93 ± 0.97	15.22 ± 0.23	4.50 ± 0.34	5.57 ± 0.15	10.95 ± 0.25	0.01 ± 0.08	0.89 ± 0.05	1.91 ± 0.18	7.60 ± 0.17	94.58 ± 1.29	4.76

a) Analysis represents glass and quench crystals (see text).
b) ΣFeO concentration in the glasses recalculated to a water-free basis (normalized to a sum of 100).

730

731

Table 3. Results of wet-chemical colorimetric iron analyses on international reference materials and in-house standards.

		this study							recommended values									
sample	description	sample weight[a] (mg)	T[b] (°C)	n[c]	$Fe^{2+}/\Sigma Fe$	(2σ)	ΣFeO (wt%)	(2σ)	ferrous FeO (wt%)	(2σ)	$Fe^{2+}/\Sigma Fe$	(2SE)	(2σ)	ΣFeO (wt%)	(2SE)	(2σ)	ferrous FeO (wt%)	(2SE)	(2σ)	ref.
international reference materials																				
BIR-1	basalt	6-7	20	9	0.82	0.03	10.20	0.21	8.35	0.35	0.82	n.a.	0.03	10.17	n.a.	0.22	8.34	n.a.	0.20	(1)
BE-N	basalt	6-7	20	3	0.61	0.01	11.53	0.22	6.98	0.26	0.58	0.01	0.06	11.55	0.05	0.63	6.74	0.08	0.60	(2)
RGM-1	calc-alkaline rhyolite	19-22	20	15	0.76	0.04	1.63	0.05	1.25	0.06	0.76	n.a.	0.06	1.67	n.a.	0.05	1.27	n.a.	0.10	(1)
RGM-1	calc-alkaline rhyolite	19-23	100	3	0.78	0.02	1.63	0.04	1.28	0.07	0.76	n.a.	0.06	1.67	n.a.	0.05	1.27	n.a.	0.10	(1)
STM-1	peralkaline nepheline syenite	10-11	20	9	0.49	0.02	4.23	0.20	2.05	0.11	0.44	n.a.	0.02	4.70	n.a.	0.18	2.09	n.a.	0.06	(1)
STM-1	peralkaline nepheline syenite	10-12	100	3	0.46	0.02	4.63	0.10	2.15	0.05	0.44	n.a.	0.02	4.70	n.a.	0.18	2.09	n.a.	0.06	(1)
GS-N	granite	15-21	20	5	0.63	0.04	2.88	0.34	1.82	0.10	0.49	0.02	0.12	3.37	0.04	0.25	1.65	0.07	0.38	(2)
GS-N	granite	15-22	100	4	0.57	0.01	3.28	0.05	1.86	0.04	0.49	0.02	0.12	3.37	0.04	0.25	1.65	0.07	0.38	(2)
GA	granite	20-21	20	5	0.61	0.01	2.28	0.11	1.39	0.06	0.52	0.02	0.11	2.55	0.05	0.38	1.32	0.04	0.18	(2)
GA	granite	20-22	100	4	0.60	0.01	2.40	0.11	1.44	0.06	0.52	0.02	0.11	2.55	0.05	0.38	1.32	0.04	0.18	(2)
AC-E	granite	20-21	20	2	0.47	0.01	2.19	0.04	1.04	0.01	0.47	0.02	0.12	2.28	0.02	0.23	1.07	0.04	0.26	(2)
AC-E	granite	20-21	100	4	0.49	0.01	2.22	0.07	1.08	0.03	0.47	0.02	0.12	2.28	0.02	0.23	1.07	0.04	0.26	(2)
in-house standards																				
PU-3[d]	andesite glass (syn.)	5-9	20	33	0.39	0.03	7.44	0.15	2.87	0.24	0.42	n.a.	0.03	7.49	0.15	0.34	3.15	n.a.	0.21	(3,4)
PU-3[d]	andesite glass (syn.)	5-9	100	4	0.40	0.02	7.20	0.44	2.86	0.28	0.42	n.a.	0.03	7.49	0.15	0.34	3.15	n.a.	0.21	(3,4)
CT-1[e]	basalt glass (syn.)	5-6	20	8	0.39	0.03	12.78	0.23	5.02	0.29	n.a.	n.a.	n.a.	12.85	0.19	0.44	n.a.	n.a.	n.a.	(4)
CA	Chlorite	1.5	20	3	0.89	0.04	39.96	1.35	35.8	1.67	0.90	n.a.	0.02	41.56	0.12	0.79	37.32	0.11	0.71	(5)
olivine	$Mg_{1.829}Fe^{2+}_{0.171}SiO_4$ (natural)	3-6	20	13	0.93	0.05	8.30	0.74	7.75	0.74	1.00	n.a.	n.a.	8.38	0.06	0.07	8.38	0.06	0.07	(4,6)
ammonium iron(II) sulfate hexahydrate	$(NH_4)_2Fe(SO_4)_2 \cdot 6H_2O$ (Merck, p.a.)	1-2	20	11	0.95	0.08	18.46	0.70	17.57	1.50	1.00	n.a.	n.a.	18.42	n.a.	n.a.	18.42	n.a.	n.a.	(6)

n.a. not available. a) Range of sample weight used for analyses. b) Decomposition temperature. c) Number of replicate analyses.

d) Electron microprobe analysis of synthetic glass CT-1 (wt%): SiO_2 47.40, Al_2O_3 14.24, ΣFeO 12.85, MgO 6.25, CaO 10.79, Na_2O 2.68, K_2O 0.32, TiO_2 3.17

e) Electron microprobe analysis of synthetic glass PU-3 (wt%): SiO_2 54.72, Al_2O_3 16.80, ΣFeO 7.49, MgO 4.15, CaO 9.00, Na_2O 3.32, K_2O 1.54, TiO_2 0.79, MnO 0.12

References for recommended values: (1) Govindaraju (1994), (2) Govindaraju (1995), (3) $Fe^{2+}/\Sigma Fe$ value calculated from ferrous iron analyses of sample Unzen-A given by Liebske et al. (2003), (4) ΣFeO values were measured by electron microprobe analysis (this study); FeO value of PU-3 calculated from ΣFeO (this study) and $Fe^{2+}/\Sigma Fe$ from Liebske et al. (2003). (5) Bertoldi et al. (2007), (6) ΣFeO (= ferrous FeO) calculated from stoichiometry.

732
733
734
735

736 **Figure captions**

737

738 **Figure 1.** UV/VIS spectra of Fe(II)-2:2'-bipyridyl solutions. Ferrous iron concentrations are
739 indicated (in µg/mL Fe). Spectra recorded in 1 cm transmission cells.

740

741 **Figure 2.** Comparison of measured $Fe^{2+}/\Sigma Fe$ ratios from this study with other studies
742 (recommended values). Open symbols refer to incomplete sample dissolution (see text). Solid
743 line represents a 1:1 correlation. Dashed lines indicate the interval ±0.03.

744

745 **Figure 3.** Oxidation state of iron as a function of H_2O mole fraction in the fluid. Lines
746 represent second order polynomials for selected datasets to illustrate the non-linear
747 relationships. Oxygen fugacity is expressed relative to the Ni-NiO buffer (ΔNNO) and the
748 given values represent the maximum log f_{O_2} values in the runs ($X^f_{H_2O} = 1$), i.e., f_{O_2} in the
749 capsule is lower at $X^f_{H_2O} < 1$.

750

751 **Figure 4 .** The dependence of the Fe^{3+}/Fe^{2+} ratio on oxygen fugacity expressed relative to the
752 NNO buffer. Note the logarithmic scaling. Alb1-1 (in parentheses) is the only sample
753 containing clinopyroxene crystals (see text). Symbols as in Figure 3.

754

755 **Figure 5.** Comparison between measured and calculated $Fe^{2+}/\Sigma Fe$ ratios from the experiments
756 and models of (a) Moretti (2005) and (b) Kress and Carmichael (1991), respectively. The
757 solid line is a 1:1 correlation and the dashed lines represent an envelope of ±0.05. Symbols as
758 in Figure 3.

759

760 **Figure 6.** Fe^{3+}/Fe^{2+} ratio as a function of log f_{O_2} in comparison with the predictions of the
761 empirical model of Kress and Carmichael (1991) (dashed lines) and the thermodynamic
762 model of Moretti (2005) (grey areas) for the phono-tephritic melt at 200 and 500 MPa. All
763 data in (a), (b) and (d) represent constant hydrogen fugacity (f_{H_2} ~0.6 bar) while for data
764 shown in (c) the hydrogen fugacity varied from 0.6 to 16.7 bar (measured values). The model
765 of Moretti (2005) takes the effect of water contents into account and the lower and upper
766 limits of the grey areas comprise the range from 0 to 10 wt% H_2O at 500 MPa (a, b) and from
767 0 to 5 wt% H_2O at 200 MPa (c, d). This range covers the measured water concentrations in
768 the experimental glasses. For comparison the experimental data of Botcharnikov et al. (2005)
769 for hydrous ferrobasaltic melts are shown (c).

770
771
772 **Figure 7.** (a) Redox state of iron in the phono-tephritic melt as a function of pressure for
773 experiments with pure H_2O fluid at intrinsic redox conditions in the IHPV (NNO+2.6). For
774 comparison the pressure dependence of the $Fe^{2+}/\Sigma Fe$ ratio calculated at 1250°C after Kress
775 and Carmichael (1991) and Moretti (2005) at given H_2O contents is shown. The
776 corresponding water contents of the experimental samples are shown in (b).

777

778

779

Figure 1

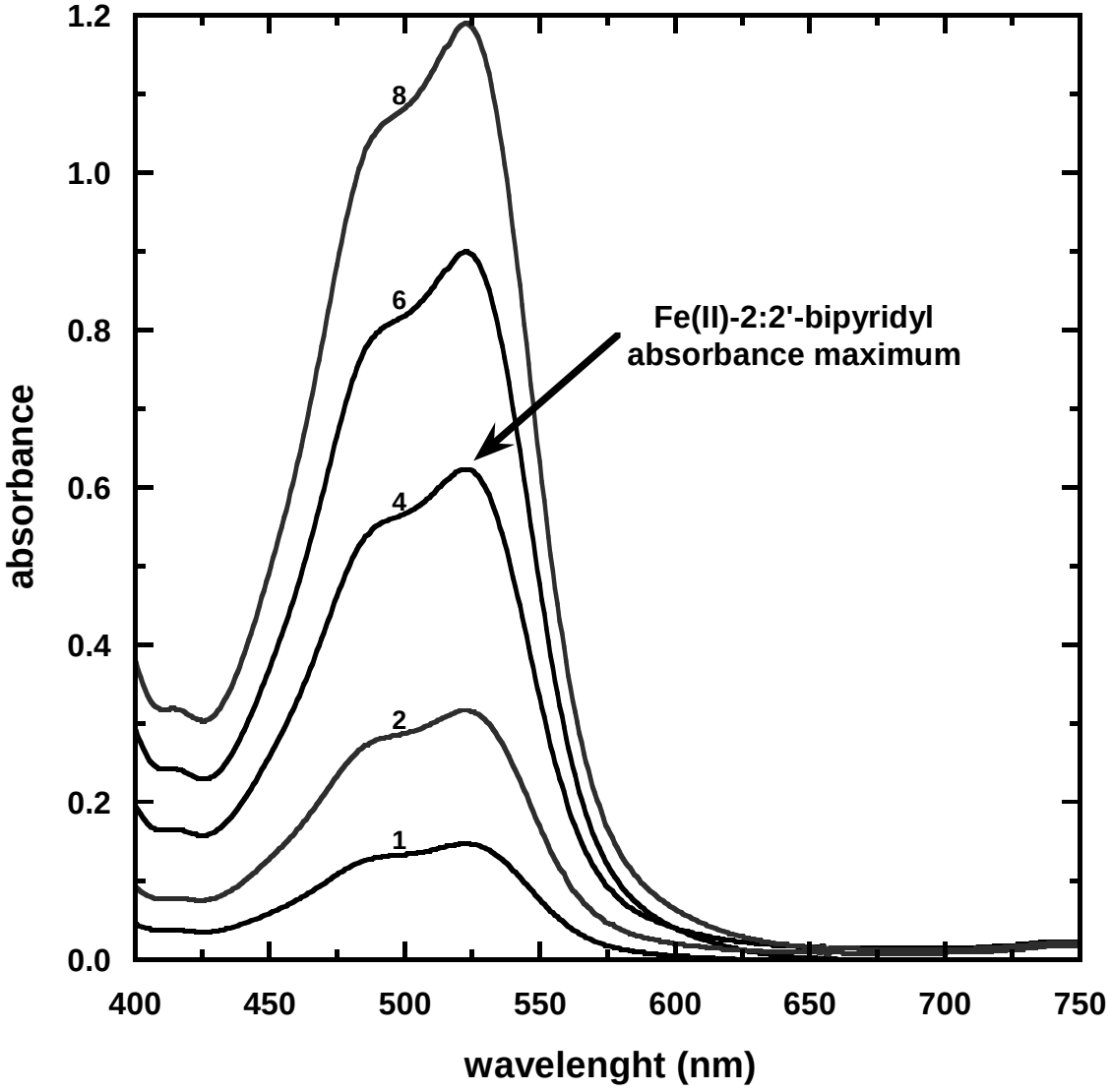
1.2
1.0
0.8
0.6
0.4
0.2
0.0
absorbance
400
450
500
550
600
650
700
750
wavelenght (nm)
8
6
4
2
1
Fe(II)-2:2'-bipyridyl
absorbance maximum

Figure 2

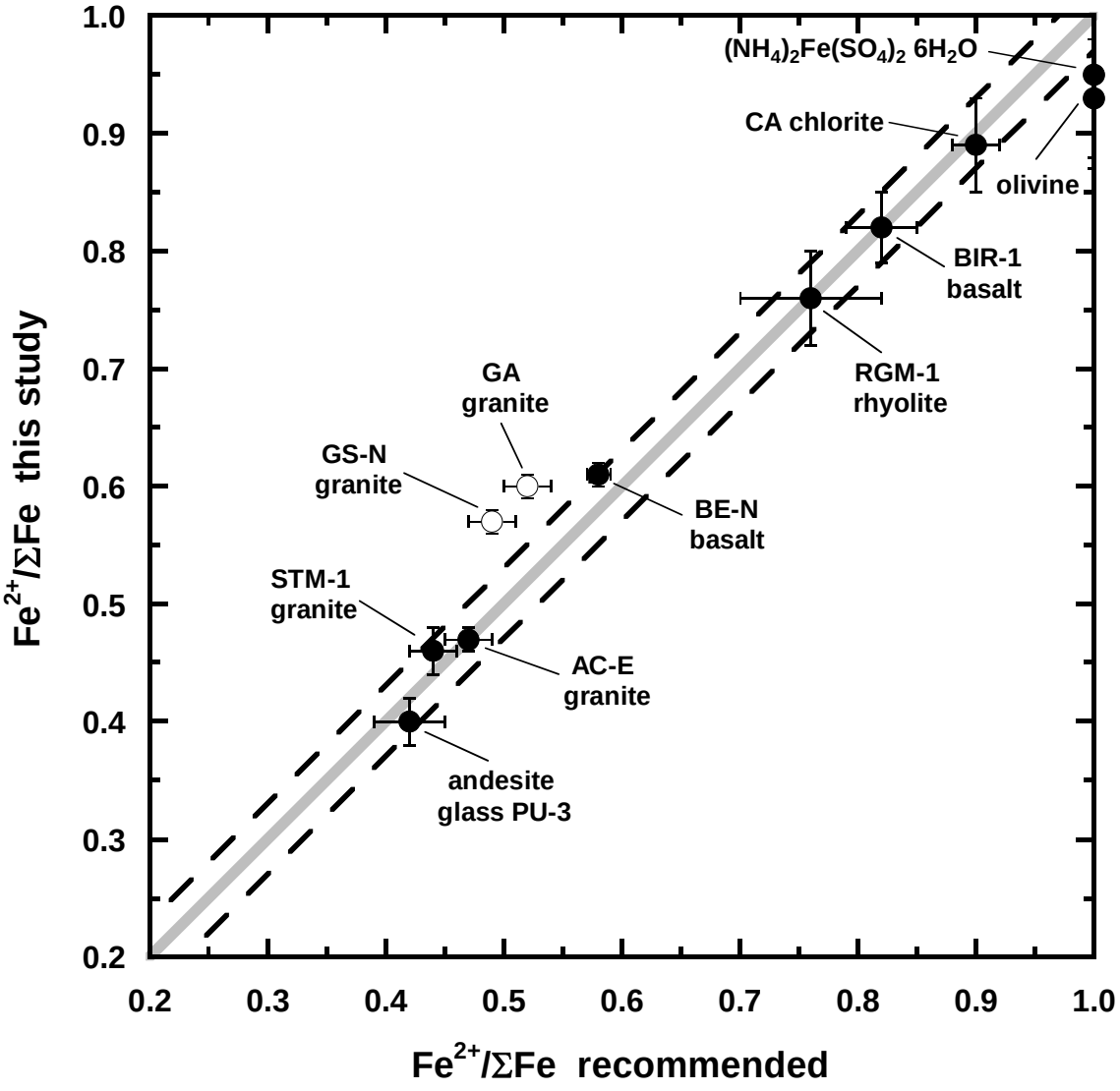
1.0
0.9
0.8
0.7
0.6
0.5
0.4
0.3
0.2
0.2
0.3
0.4
0.5
0.6
0.7
0.8
0.9
1.0
Fe2+/ΣFe this study
Fe2+/ΣFe recommended
(NH4)2Fe(SO4)2 6H2O
CA chlorite
olivine
BIR-1
basalt
RGM-1
rhyolite
GA
granite
GS-N
granite
BE-N
basalt
STM-1
granite
AC-E
granite
andesite
glass PU-3

Figure 3

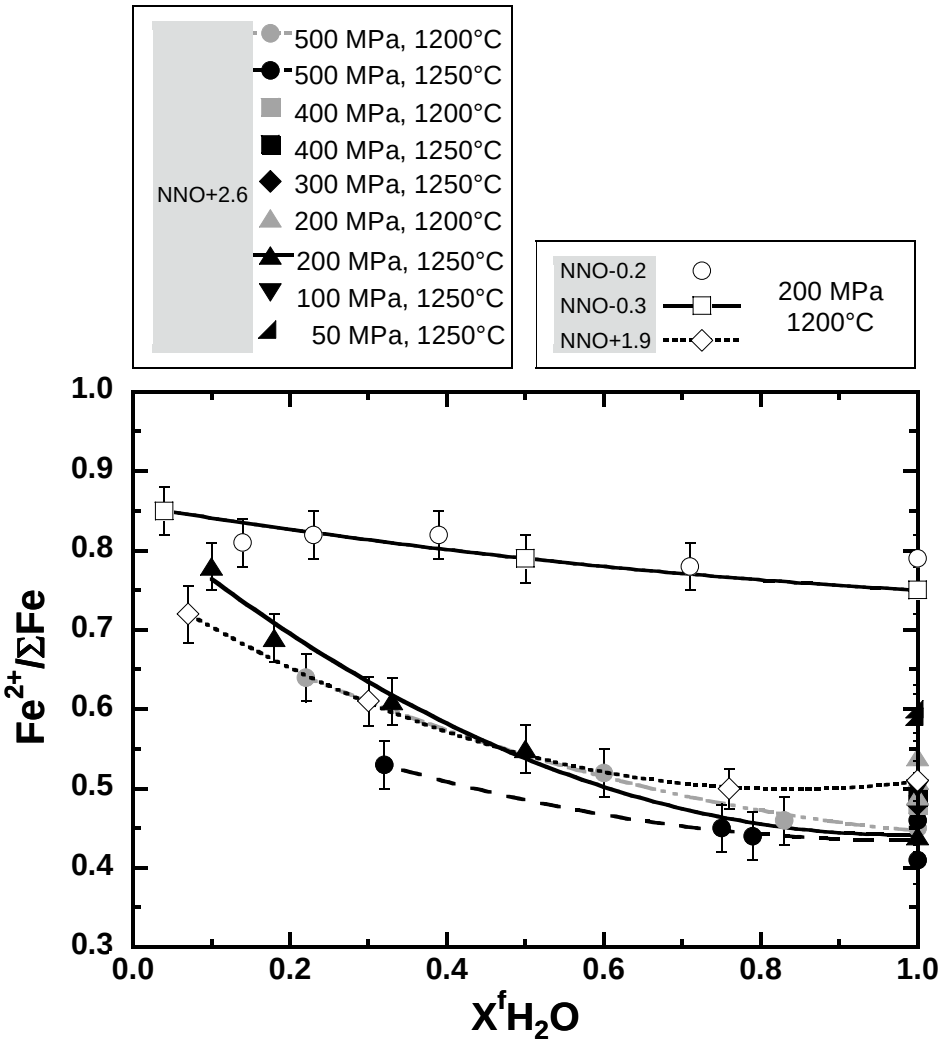
NNO+2.6
500 MPa, 1200°C
500 MPa, 1250°C
400 MPa, 1200°C
400 MPa, 1250°C
300 MPa, 1250°C
200 MPa, 1200°C
200 MPa, 1250°C
100 MPa, 1250°C
50 MPa, 1250°C
NNO-0.2
NNO-0.3
NNO+1.9
200 MPa
1200°C
Fe2+/ΣFe
XfH2O
1.0
0.9
0.8
0.7
0.6
0.5
0.4
0.3
0.0
0.2
0.4
0.6
0.8
1.0

Figure 4

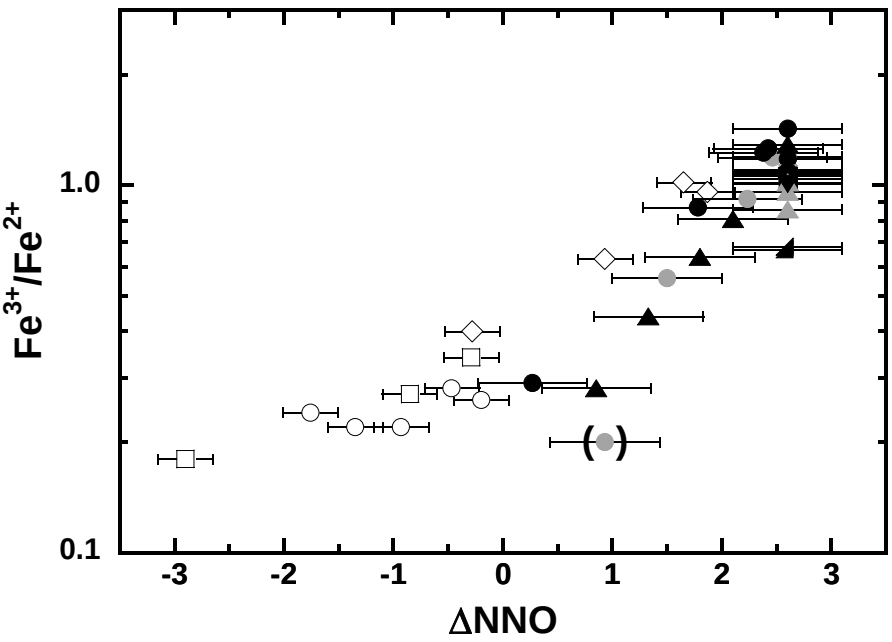

Figure 5

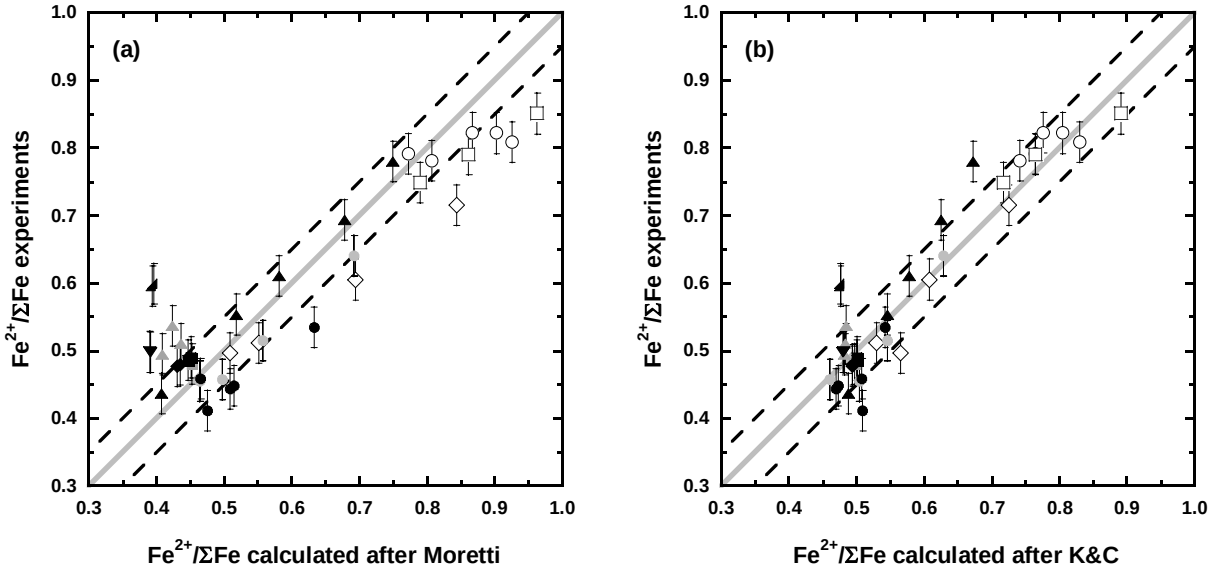
(a)
(b)
Fe2+/ΣFe experiments
Fe2+/ΣFe calculated after Moretti
Fe2+/ΣFe calculated after K&C
0.3
0.4
0.5
0.6
0.7
0.8
0.9
1.0

Figure 6

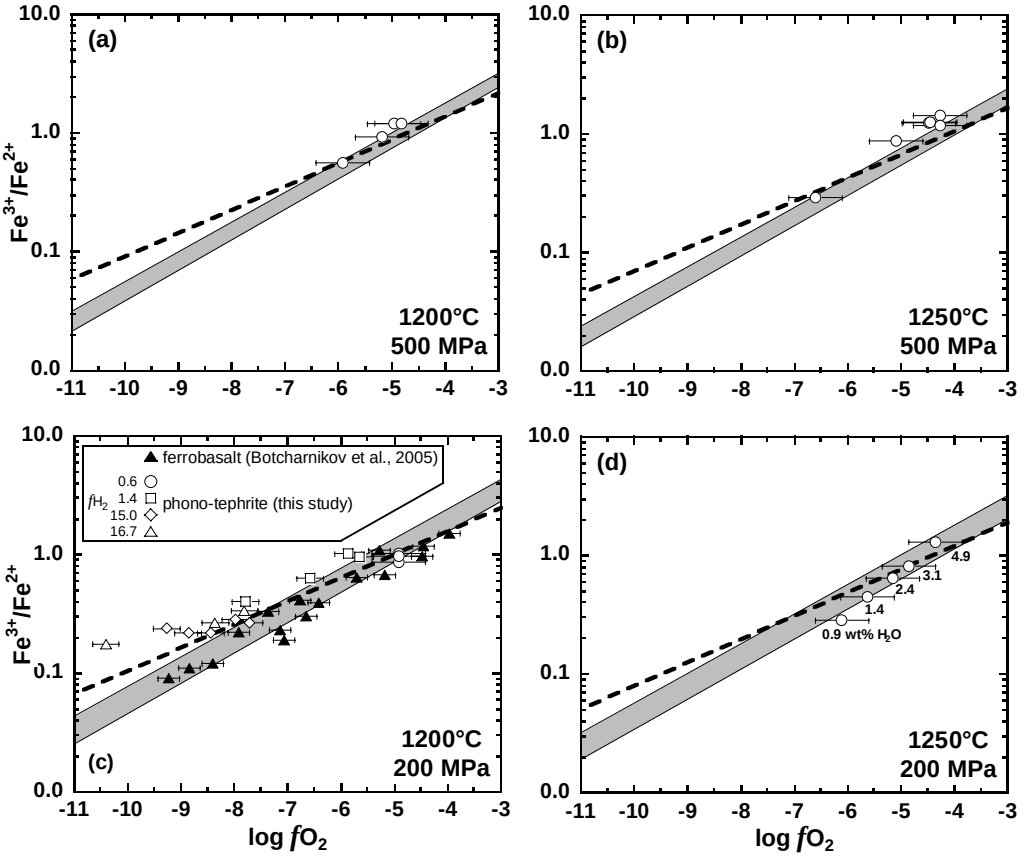
(a)
1200°C
500 MPa
(b)
1250°C
500 MPa
(c)
1200°C
200 MPa
(d)
1250°C
200 MPa
ferrobasalt (Botcharnikov et al., 2005)
fH_2
0.6
1.4
15.0
16.7
phono-tephrite (this study)
4.9
3.1
2.4
1.4
0.9 wt% H_2O
Fe^{3+}/Fe^{2+}
log fO_2
10.0
1.0
0.1
0.0
-11
-10
-9
-8
-7
-6
-5
-4
-3

Figure 7

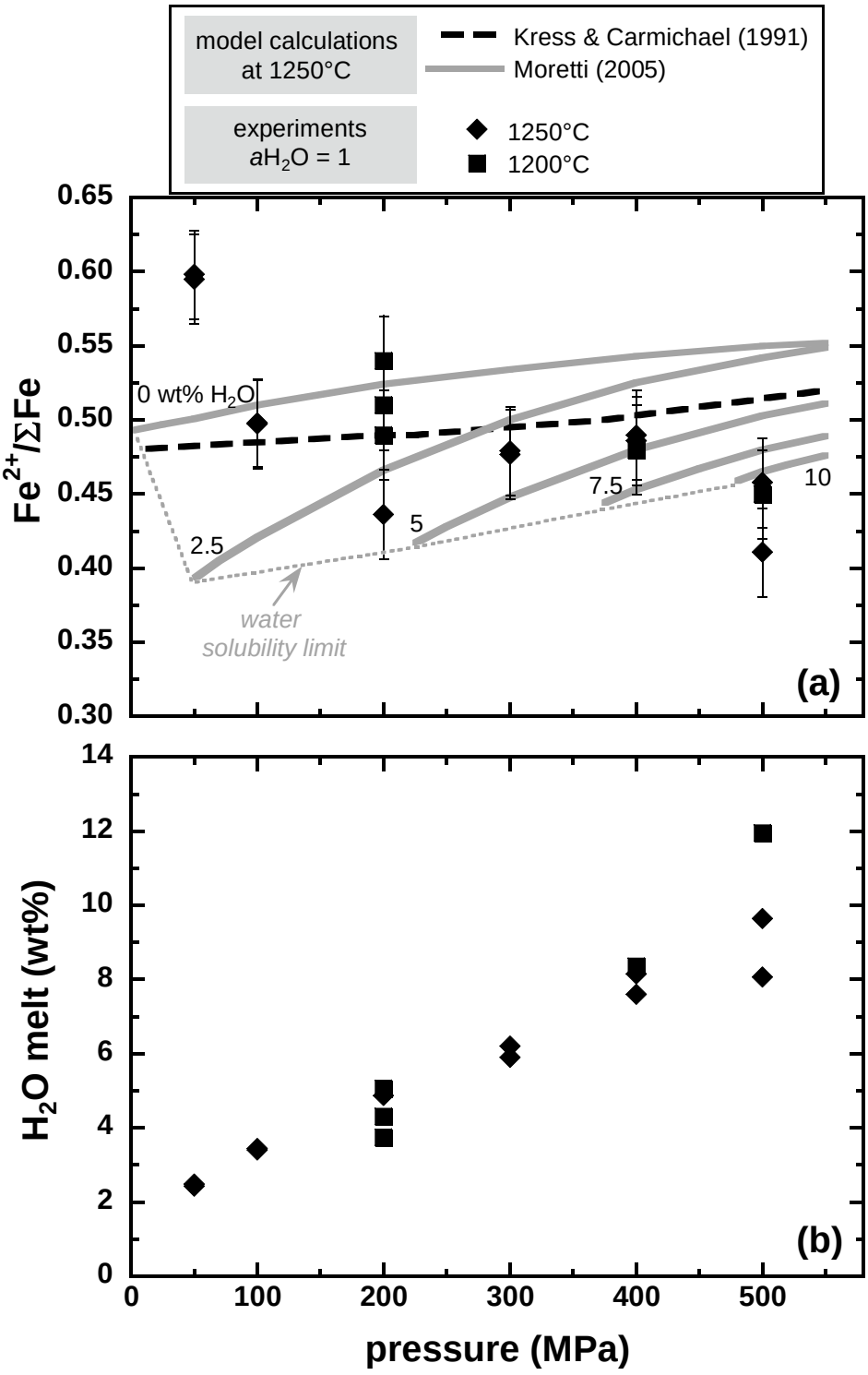
model calculations at 1250°C
Kress & Carmichael (1991)
Moretti (2005)
experiments $aH_2O = 1$
1250°C
1200°C
$Fe^{2+}/\Sigma Fe$
0.65
0.60
0.55
0.50
0.45
0.40
0.35
0.30
0 wt% H_2O
2.5
5
7.5
10
water solubility limit
(a)
H_2O melt (wt%)
14
12
10
8
6
4
2
0
0
100
200
300
400
500
pressure (MPa)
(b)